The Massive Star Population in the Giant H II Region Tol 89 in NGC 5398*

Fabrizio Sidoli[1]†, Linda J. Smith[1] and Paul A. Crowther[2]
[1] *Department of Physics and Astronomy, University College London, London WC1E 6BT, UK*
[2] *Department of Physics and Astronomy, University of Sheffield, Sheffield S3 7RH, UK*

ABSTRACT
We present new high spectral resolution VLT/UVES spectroscopy and archival HST/STIS imaging and spectroscopy of the giant H II region Tol 89 in NGC 5398. From optical and UV HST images, we find that the star-forming complex as a whole contains at least seven young compact massive clusters. We resolve the two brightest optical knots, A and B, into five individual young massive clusters along our slit, A1–4 and B1 respectively. From Starburst99 (Leitherer et al.) UV spectral modelling, and nebular Hβ equivalent widths in the optical, we derive ages that are consistent with the formation of two separate burst events, of $\sim 4 \pm 1$ Myr and < 3 Myr for knots A (A1–4) and B (B1), respectively. An LMC metallicity is measured for both knots from a nebular line analysis, while nebular He II 4686 is observed in knot B and perhaps in knot A. We detect underlying broad wings on the strongest nebular emission lines indicating velocities up to 600 km s^{-1}. From UV and optical spectroscopy, we estimate that there are $\sim$95 early WN stars and $\sim$35 early WC stars in Tol 89-A, using empirical template spectra of LMC WR stars from Crowther & Hadfield, with the WC population confined to cluster A2. Remarkably, we also detect a small number of approximately three mid WNs in the smallest (mass) cluster in Tol 89-A, A4, whose spectral energy output in the UV is entirely dominated by the WN stars. From the strength of nebular Hβ, we obtain N(O) $\sim$690 and 2800 for knots A and B, respectively, which implies N(WR)/N(O)$\sim$0.2 for knot A. We also employ a complementary approach using Starburst99 models, in which the O star content is inferred from the stellar continuum, and the WR population is obtained from spectral synthesis of optical WR features using the grids from Smith et al. We find reasonable agreement between the two methods for the O star content and the N(WR)/N(O) ratio but find that the WR subtype distribution is in error in the Starburst99 models, with far too few WN stars being predicted. We attribute this failure to the neglect of rotational mixing in evolutionary models. Our various modelling approaches allow us to measure the cluster masses. We identify A1 as a super star cluster (SSC) candidate with a mass of ~ 1–2×10^5 M$_\odot$. A total mass of $\sim 6 \times 10^5$ M$_\odot$ is inferred for the ionizing sources within Tol 89-B.

Key words: stars − Wolf-Rayet: stars − O stars: galaxies − starbursts: galaxies − massive star population: giant H II regions − Tol 89.

1 INTRODUCTION

Giant H II regions (GHRs) are characterised by their large sizes (up to ≈ 1 kpc), supersonic gas motions (Melnick, Tenorio-Tagle & Terlevich 1999) and high Hα luminosities (10^{38}–10^{41} ergs s^{-1}; Kennicutt 1984). A review of their properties is given by Shields (1990). The presence of GHRs in galaxies denotes sites of recent, intense episodes of massive star formation. The nearest extragalactic GHR is 30 Doradus in the Large Magellanic Cloud (LMC) which hosts a compact star cluster (R136) of mass ~ 2–6×10^4 M$_\odot$ (Hunter et al. 1995) as the main ionizing source. Conversely, another nearby GHR, NGC 604 in M33, is of similar size but contains multiple OB associations rather than a central massive cluster. The mechanism(s) which ultimately determines whether a cluster or a complex of OB associations

is formed when an intense star-forming event occurs is unclear. Elmegreen & Efremov (1997) suggest that clusters are formed in preference to loose associations in high pressure interstellar environments. Clusters with masses as high as 10^5 to $\sim 10^8$ M$_\odot$ (Maraston et al. 2004) – often termed young massive clusters (YMCs), or super star clusters (SSCs) – are observed in the extreme environments of starburst galaxies and galaxy mergers (e.g. Whitmore 2003); the most luminous and compact of which show similar properties to older globular clusters (GCs) such as those observed in the Milky Way (e.g. Holtzman et al. 1992; Whitmore et al. 1997; Schweizer & Seitzer 1998; Bastian et al. 2006, see also Larsen 2004 for a review). This has led to the suggestion that YMCs may represent the young counterparts of old GCs (e.g. Ashman & Zepf 1992) and may offer insight into the formation and evolution of GCs in the local universe.

Recently, Chen, Chu & Johnson (2005) have studied the cluster content of three GHRs (NGC 5461, NGC 5462 and NGC 5471) in M 101. They find that they contain clusters similar to R136 in mass rather than the more massive SSCs, although they note that the three R136-like clusters in NGC 5461 may merge to form an SSC. Overall, they find evidence for a link between the molecular cloud distribution and the cluster luminosity function in the sense that a diffuse distribution produces more lower mass clusters, in support of the hypothesis that massive clusters are formed in high pressure environments.

The giant H II region Tol 89 (Smith et al. 1976) is located at the south-western end of the bar in the late-type barred spiral (Sdm) galaxy NGC 5398 (Durret et al. 1985). A Digital Sky Survey image of this galaxy is shown in Fig. 1; Tol 89 is conspicuous in being the only large massive star-forming complex present in the entire galaxy. Tol 89 has an extent of $\approx 24'' \times 18''$ or 1.7×1.2 kpc and an absolute blue magnitude of -14.8, (assuming a distance of 14.7 Mpc based on $H_0 = 75$ km s^{-1}Mpc^{-1}; Schaerer et al. 1999) which makes it one of the most impressive GHRs known.

The presence of Wolf-Rayet (WR) stars in Tol 89 was first reported by Durret et al. (1985) who detected a broad emission bump at $\lambda 4650$. Schaerer, Contini & Kunth (1999) identified broad features of N III 4640, He II 4686, and very strong C IV 5808, suggesting the presence of both late-type WN (WNL) and early-type WC (WCE) stars in Tol 89. From a detailed spatial analysis, they find an offset between the continuum and nebular lines, suggesting a complex star-forming region. Johnson, Indebetouw & Pisano (2003) obtained radio observations of Tol 89 and discovered an unresolved thermal radio source with a Lyman continuum flux of $\sim 4500 \times 10^{49}$ s^{-1}, equivalent to an SSC with a mass of 10^6 M$_\odot$ if the source is a single cluster. In terms of radio luminosity, they find that Tol 89 is among the most luminous radio H II regions so far observed and is comparable to the GHR NGC 5471 in M 101. Finally, Tol 89 was one of the objects in the survey of Chandar et al. (2004) to measure the WR content of actively star-forming regions through ultraviolet (UV) spectroscopy obtained with the *Hubble Space Telescope* (HST) Space Telescope Imaging Spectrograph (STIS).

In this paper, we examine the massive stellar content of Tol 89 through an analysis of archival HST images and UV spectroscopy, and high resolution optical spectroscopy obtained with the *Very Large Telescope* (VLT). We show that Tol 89 is a young, very massive star-forming complex
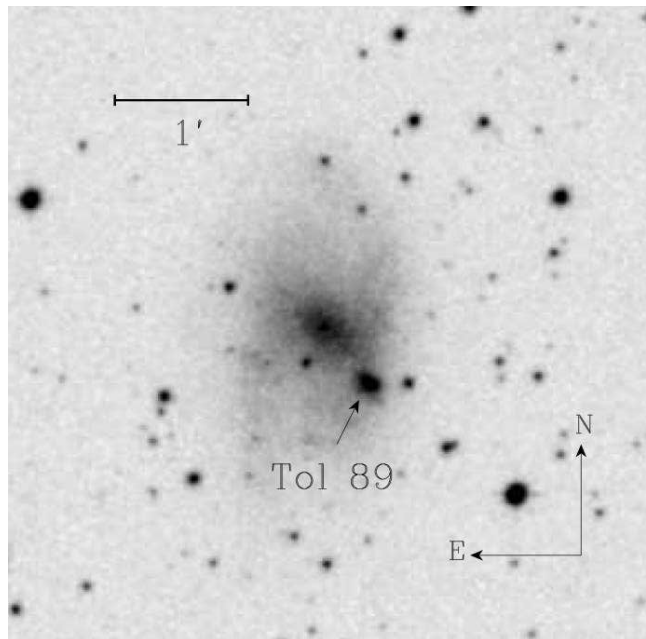
Figure 1. Digital Sky Survey R-band image of NGC 5398 showing the location of the GHR Tol 89. At the adopted distance of 14.7 Mpc, $1'$ corresponds to ≈ 4 kpc. The field of view is 5×5 arc minutes.

with at least seven young compact massive clusters. The fact that Tol 89 is located at the end of the bar in NGC 5398 indicates it may have been formed through gas inflow in a high pressure environment, although Johnson et al. (2003) suggest that the weak bars found in late-type galaxies are not strong enough to generate the required gas inflow.

The paper is structured as follows. The observations and reductions are presented in Section 2. In Section 3 we describe the spectra and in Sections 4 and 5 we derive the properties of the knots and their ionizing clusters. In Section 6 we estimate the massive star content using empirical and synthesis techniques. Finally, in Sections 7 and 8 we discuss and summarise our results.

2   OBSERVATIONS

We have obtained high spectral resolution *UV-Visual Echelle Spectrograph* (UVES)+VLT echelle spectroscopy of the brightest optical knots in the giant H II region Tol 89. We supplement this dataset with archival HST imaging and spectroscopy obtained using the STIS CCD and FUV-MAMA detectors in the optical and UV respectively (Proposal ID 7513; C. Leitherer, P.I.). The UV spectroscopic data are also presented in Chandar et al. (2004). A summary of the observations is given in Table 1. All the HST archive data were processed using the standard CALSTIS data reduction pipeline.

2.1   Imaging

2.1.1   Reduction

Optical and UV images were obtained on 1999 February 19 using the MIRVIS/STIS CCD and MIRFUV/FUV-MAMA
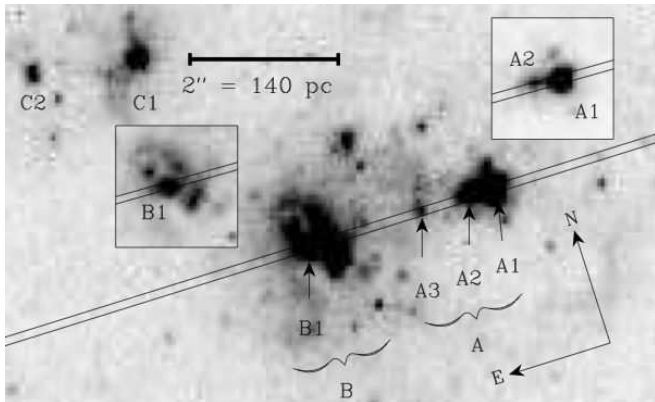
Figure 2. STIS MIRVIS (λ_{cen}=7230 Å) image showing the position and orientation (PA = -90°) of the optical STIS slit, of size $52'' \times 0\rlap{.}''1$ arc seconds. Clusters A1-3, B1, C1 and C2 are indicated (see Section 2.1.2). At the adopted distance of 14.7 Mpc, $1''$ corresponds to ≈ 70 pc. The stretch of the image has been set so as to highlight the position of cluster A3. The insets show the regions around A1 and A2 (top right) and B1 (centre left) at different stretches to highlight better these clusters.
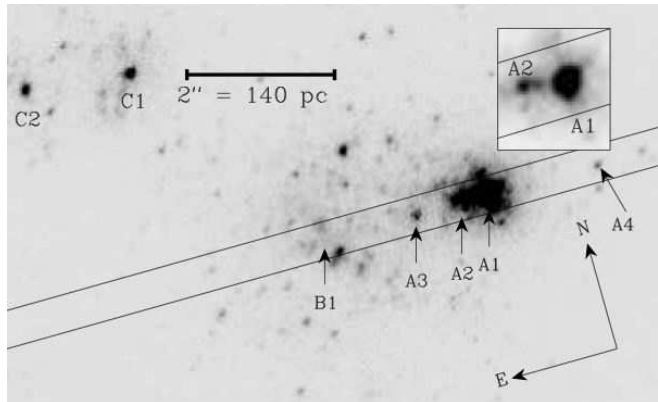
Figure 3. STIS MIRFUV (λ_{cen}=1480 Å) image showing the position and orientation (PA = -90°) of the UV STIS slit, of size $52'' \times 0\rlap{.}''5$. Clusters A1-4, B1, C1 and C2 are indicated (see Section 2.1.2). At the adopted distance of 14.7 Mpc, $1''$ corresponds to ≈ 70 pc. The stretch of the image has been set so as to highlight the position of clusters A3 and A4. The inset shows the region around clusters A1 and A2. Note, cluster B1 is almost completely obscured in the UV.
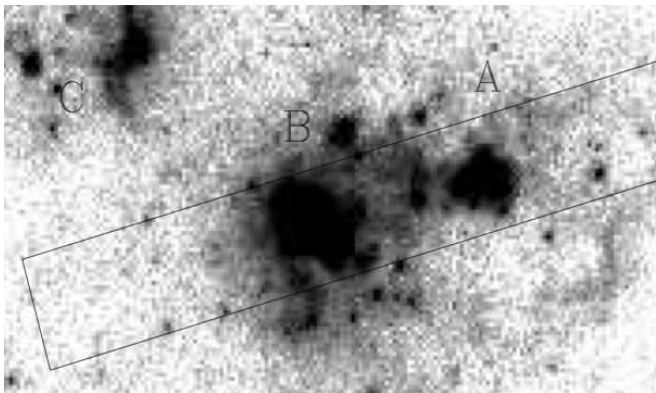
Figure 4. STIS MIRVIS (λ_{cen}=7230 Å) image showing the position and orientation (PA = 90°) of the UVES slit, of size $1\rlap{.}''4 \times 10''$. Knots A, B and C are indicated (see Section 2.1.2). The orientation and scale are as in Figs. 2 and 3.

longpass filters/detectors. The optical dataset consists of four image sets. Before combining, we first used intensity histograms of the images to determine a threshold value for the cold pixels, below which all pixels were flipped to high values. These were subsequently removed, along with cosmic rays and hot pixels, using the IRAF/STSDAS cosmic ray rejection (OCCREJ) task upon combining the images. The resulting images were then geometrically corrected using the X2D task. Remaining hot pixels were removed using the Laplacian cosmic ray identification algorithm, L.A.Cosmic (van Dokkum 2001). In Figs. 2 and 3 we show the optical and UV STIS images of Tol 89, with the slit positions of the STIS spectroscopy superimposed (see Section 2.2.1). Similarly in Fig. 4 we show the optical STIS image with the slit position of the UVES spectroscopy overlaid (Section 2.2.2).

2.1.2   Optical and UV morphology

Tol 89 is a young massive star forming complex as shown by the optical and UV STIS images in Figs. 2 and 3. It

comprises three distinct knots of star formation that we label A, B and C in order of decreasing (optical) brightness. With the high spatial resolution of HST, we are able to resolve each individual knot into multiple cluster components.

Along the optical STIS slit, the boundary between A and B is defined by the mid-point between the brightest optical component in each knot. We then identify the clusters in order of decreasing brightness along the slit, with 1 being the brightest (see Figs. 2 and 3). The UV counterparts to each cluster were then identified in the FUV-MAMA image. The separation between the clusters, as measured from the optical STIS image, are as follows: A4→A1: $1\rlap{.}''53$ (107 pc); A1→A2: $0\rlap{.}''32$ (22 pc); A2→A3: $0\rlap{.}''69$ (49 pc); and A3→B1: $1\rlap{.}''51$ (106 pc). The projected separations in parsecs are given in parentheses, where $1'' \approx 70$ pc (assuming a distance of 14.7 Mpc based on $H_0 = 75$ km s^{-1}Mpc^{-1}; Schaerer et al. 1999).

Knot A is made up of multiple clusters that are bright in both the optical and the UV, and dominated by a young compact cluster which we denote as A1. Whilst knot B is also optically bright and complex it is much fainter than A in the UV. It is also the location of the impressive thermal radio source discovered by Johnson et al. (2003). From the STIS UV image (Fig. 3) we can see that knot C contains two young compact massive clusters which we denote as C1 and C2; where C1 is the location of the north-eastern spur of thermal radio emission identified by Johnson et al. 2003 (see their fig. 4).

Durret et al. (1985) identify two regions in Tol 89 that they denote as X and C, where C is their centre of Tol 89. We identify our knot C with their region X and their centre of Tol 89 with our knots A and B. Within the centre of Tol 89, Schaerer et al. (1999) identify an area with maximum nebular intensity (= our B), offset by ~ 2 arc seconds to the east of the region with maximum continuum intensity and

Table 1. Summary of the observations. The HST+STIS imaging and spectroscopy (Proposal ID 7513, C. Leitherer, P.I.) have been obtained from the HST archive.

Detector	Filter	λ_{cen} (Å)	FWHM (Å)	PA (°)	Aperture Size (″)	Pixel Scale (″pix^{-1})	Total Exp. (s)/ Imsets
		HST+STIS Imaging, 1999 February 19					
FUV-MAMA	MIRFUV	1480	280	106.7	25×25	0.0246	900/1
CCD	MIRVIS	7230	2720	106.7	28×50	0.0507	240/4

Detector	Grating/ Setting	λ_{cen} (Å)	λ_{range} (Å)	Resolution (Å)	Dispersion (Åpix^{-1})	PA (°)	Slit Size (″)	Pixel Scale (″pix^{-1})	Total Exp. (s)/ Imsets
			HST+STIS Spectroscopy, 2000 March 20-21						
FUV-MAMA	G140L	1500	1150-1700	3.1	0.58	89.0	52×0.5	0.0246	11620/4
CCD	G430L	3200	2900-5700	4.9	2.73	89.1	52×0.1	0.0507	810/2
CCD	G750M	6581	6295-6867	1.0	0.56	89.1	52×0.1	0.0507	825/2
			UVES+VLT Spectroscopy, 2004 May 6						
EEV CCD	Dichroic #1	3460	3030-3880	0.19	0.035	90.0	1.4×10	0.246	2850/2
EEV CCD	Dichroic #2	4370	3730-4990	0.22	0.044	90.0	1.4×10	0.246	2850/2
EEV/MIT-LL CCD	Dichroic #1	5640	4580-6680	0.36/0.29^a	0.049/0.040^a	90.0	1.4×11	0.182	2850/2
EEV/MIT-LL CCD	Dichroic #2	8600	6660-10600	0.63/0.45^a	0.075/0.060^a	90.0	1.4×12	0.170	2850/2

^{a} Resolutions and dispersions are for CCD1/CCD2

the location of the WR emission (= our A; see also their fig. 5[1]).

2.2 Spectroscopy

2.2.1 STIS spectroscopy

The two-dimensional STIS spectroscopic data were obtained over two visits on 2000 March 20-21 using the G430L and G750M gratings and the STIS CCD detector for the optical regime, and the G140L grating and the STIS FUV-MAMA detector for the UV. The slits were centred on the brightest cluster (=A1) at co-ordinates of $\alpha = 14^h01^m19\overset{s}{.}92$; $\delta = -33^h04^m10\overset{''}{.}7$ (J2000). The respective slit sizes are $52'' \times 0\overset{''}{.}1$ and $52'' \times 0\overset{''}{.}5$ and are shown in Figs. 2 and 3. Further details are given in Table 1. The image sets (two for each optical grating and four for the UV) were combined using the method described in Section 2.1.1 and rectified, wavelength and absolutely flux calibrated using the x2D task. From measurements of the FWHM of Gaussian fits to the unresolved Hβ and C II 1335 lines in the G430L and G140L spectra of B1, we obtain spectral resolutions of 4.9Å and 3.1Å respectively, or 1.8 pixels, giving a resolution of 1.0Å for the G750M grating.

From the UV spectral image, we identify five regions for extraction which we denote as A1, A2, A3, A4 and B1 in Fig. 2 (see Section 2.1.2). The extraction widths correspond to 0.23, 0.12, 0.19, 0.19 and 0.30 arc seconds, respectively. Note that in Fig. 3 the bright UV source in the vicinity of B1 is actually the UV counterpart to the optical point source that lies below, and just outside of the narrower optical slit (see leftmost inset of Fig. 2). For this reason we make careful considerations regarding the extraction width of B1 to ensure that there is as little contamination from this source as possible.

For the optical we extract three regions A1+2, A3 and B1, with the extraction widths being defined by the full width at ~10 per cent of the peak of the intensity profile at Hα. These extraction widths, corresponding to 0.55, 0.40 and 1.13 arc seconds respectively, were then applied to the G430L grating spectra. Note, regions A1 and A2 are barely resolved in the optical STIS 2D spectral image and hence are extracted as a single source object while cluster A4 is not detected above the background noise. Background subtraction was performed by selecting regions of sky free of nebular emission. No correction for slit losses have been made.

2.2.2 UVES spectroscopy

Echelle spectra of Tol 89 were obtained in service mode on 2004 May 6 with UVES (D'Odorico et al. 2000) at the VLT Kueyen Telescope (UT2) in Chile (Proposal ID 73.B-0238A, L. J. Smith, P.I.). UVES is a two arm cross-dispersed echelle spectrograph with the red arm containing a mosaic of an EEV and a MIT-LL CCD. The blue arm has a single EEV

[1] Note that the orientation in fig. 5 of Schaerer et al. 1999 is incorrect. North points towards the top right corner of their middle panel rather than the top left. Thus, the peak in nebular intensity (our knot B) is offset by ~ 2 arc seconds to the east of the continuum intensity peak (our knot A) rather than south, as is suggested in their figure.

CCD; all three CCDs have a pixel size of 15μm. Simultaneous observations in the blue and the red were made using the standard setups with dichroic #1 (346+564 nm) and dichroic #2 (437+860 nm), covering an almost continuous wavelength region from 3100–10 360Å; the regions between 5610–5670Å and 8540–8650Å were not observed as a result of the gap between the two CCDs in the red arm. The slit was oriented at a position angle of 90 deg to pass through the two brightest knots in Tol 89, hereafter A and B when discussing the UVES data (see Fig. 4). The slit width was set at 1″4, giving a resolving power of $\sim$ 30 000 in the blue and $\sim$ 28 000 in the red. The pixel scales for 1×1 binning are shown in Table 1.

At the time of the observations the conditions were clear and the seeing was typically better than 1″2. A total integration time of 47.5 min. was divided into two equal length exposures to prevent saturation of the brightest nebular lines (Hα, Hβ and the [O III] $\lambda\lambda$4959, 5007). Observations of the spectrophotometric standard Feige 67 were also made using the same set up for the purpose of performing flux calibrations. Spectra of Th-Ar comparison arcs were obtained to perform wavelength calibrations.

The data were reduced according to the standard CCD and echelle reduction procedures within IRAF using the CC-DRED and ECHELLE packages. This included the subtraction of a bias level determined from the overscan region, bias subtraction, division by a normalised flat field and bad pixel correction. Images were cleaned of cosmic rays using L.A.Cosmic (van Dokkum 2001). The echelle orders were extracted using widths set to 2.4 and 3.6 arc seconds for knots A and B respectively and wavelength calibrated, atmospheric extinction corrected and flux calibrated. Resolutions – as measured from the FWHM of Gaussian profile fits to the Th-Ar arc lines – and dispersions are given in Table 1.

3 DESCRIPTION OF THE SPECTRA

3.1 STIS UV

The velocity corrected ($V_{\rm hel} \approx$ 1230–1240 km s^{-1}; see Section 5) UV spectra of clusters A1–4 and B1 are shown in Fig. 5; the characteristics of stars with strong stellar winds due to the presence of P Cygni profiles of Si IV 1400, N V 1240 and C IV 1550 can be seen. In the case of A3, the narrow and resolved Si IV 1400 profile is suggestive of late-type O supergiants.

Since O stars do not show strong He II 1640 emission, its presence in A1, A2 and A4 can be attributed to the winds from WN stars. In A2 the emission strength of the C IV 1550 feature, which is greater than He II 1640, suggests that WC stars are also present, while the non detection of He II 1640 emission in A3 and B1 would suggest an absence of WRs. In cluster A4 we appear to detect N IV] 1486 emission from mid-WN stars and note that its UV spectral appearance bares a close resemblance to that of a mid-WN star (see fig. 2 of Crowther & Dessart 1998).

The UV STIS data are also presented in fig. 1 of Chandar et al. (2004), who used a larger aperture width of 81 pixels to obtain their 1D spectrum of the region they denote as Tol 89-1. Their extraction comprises our regions A1 and A2, plus diffuse inter-cluster emission and also shows
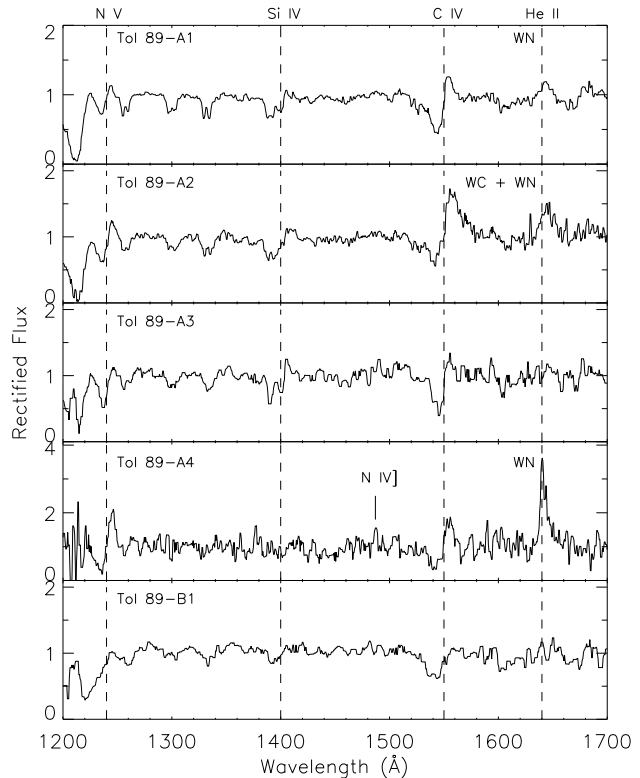

Figure 5. Velocity corrected STIS FUV-MAMA G140L spectra showing the extractions of cluster A1, A2, A3, A4 and B1 (*top, 2nd, 3rd, 4th* and *bottom* panels respectively). P Cygni profiles due to the winds of massive O and WN stars are identified: Si IV 1400 (O supergiants), N V 1240 and C IV 1550 (O stars) and He II 1640 (WN). In the case of A2, the strength of the C IV 1550 feature, which exceeds that of He II 1640, suggests the presence of WC stars.

the P Cygni profiles of N V 1240, Si IV 1400, and C IV 1550, as well as He II 1640 emission from WN stars. Our smaller, individual extractions of A1 and A2 ($\sim$ 9 and 5 pixels respectively) have allowed for different WR populations (WN and WC) to be identified in the individual clusters. From the spectrum of Tol 89-1 shown in fig. 1 of Chandar et al. the presence of WC stars is ambiguous and thus only a WN population can be inferred from their extraction.

3.2 STIS optical

The optical spectrum of A1+2 shows a very blue continuum with very weak emission lines of Hα, Hβ, [O III] 4959, 5007 and [N II] 6548/84. The portion of the G430L spectrum in the region of He II 4686 is shown in Fig. 6a; we identify a possible nebular He II 4686 component. The FWHM is comparable to that of the unresolved [O III] 5007 emission line (cf 7.0±1.8 and 6.7±1.0 Å respectively). We briefly discuss the origin of this emission in Section 7.

Clusters A3 and B1 also show emission lines of Hα, Hβ and [O III] 4959, 5007; although they are weak in A3. In addition to these lines, B1 shows weak emission lines of [O II] 3727, Hγ and Hδ. Both A3 and B1 are significantly reddened compared to A1+2; no WR emission features are detected, in agreement with the UV STIS spectra (see Fig. 5).
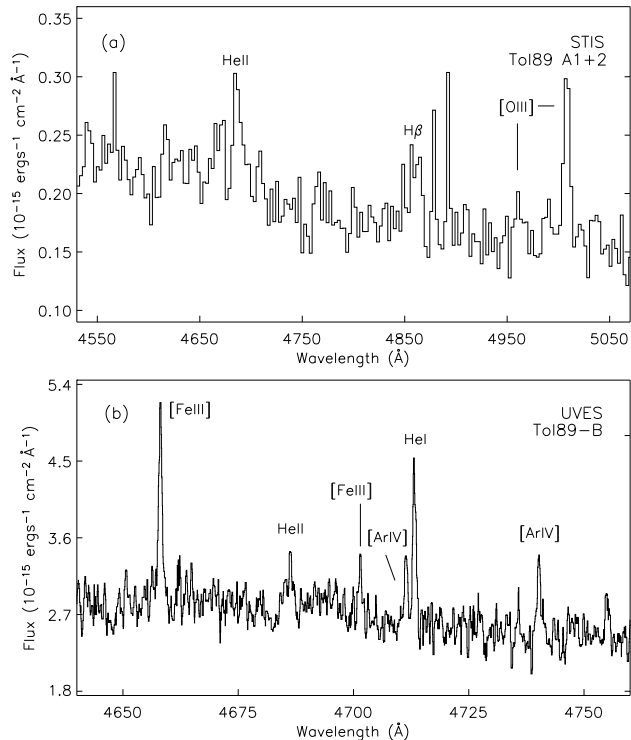
Figure 6. Velocity corrected STIS G430L spectrum of A1+2 (*top*) and UVES+VLT spectrum of B (*bottom*) showing possible *nebular* He II 4686 emission. Nebular lines of Hβ and [O III] in A1+A2, and He I, [Fe III] and [Ar IV] in region B are also identified.

3.3   UVES

The high S/N, high spectral resolution UVES data for regions A and B are shown in Figs. 7 and 8 respectively over the wavelength range of 3600–7400 Å. The spectra are rich in emission line features typical of H II regions. The strongest emission lines, those of Hα, Hβ, [O II] 3726/29, 7319/30, [O III] 4959, 5007, [N II] 6548/84, and [S II] 6716/31, exhibit a broad component resulting in extended wings. In the case of region A, the narrow components of these emission lines are split into two velocity components (denoted as V1 and V2). Both spectra show little or no stellar absorption in the Balmer lines. Metal lines due to an older population of stars are also absent and imply that regions A and B consist of a young population of stars with very similar ages. An analysis of the nebular lines is presented in Section 5.

    Regarding stellar features, we confirm the observations made by Schaerer et al., detecting broad WR emissions in knot A at $\lambda4640$ (the blue bump) and $\lambda5808$ (the yellow bump), see Figs. 7 and 9. The blue bump is a blend of *nebular* [Fe III] 4658 and *stellar* N V 4620, N III 4640, C III /C IV $\lambda4650/58$ and He II 4686, suggesting the presence of both early (WNE) and late-type (WNL) nitrogen-rich WR stars. The equivalent width of the blue bump is ≈ 11Å, with $\lambda4686$ contributing ≈ 3Å. We also detect broad (FWHM ~ 80 Å) C IV 5808 emission from WC stars with an equivalent width of ~ 12 Å.

    In region B only *nebular* lines of [Fe III] 4658, 4701, [Ar IV] 4711/40 and He I 4713 are present in the region of the blue bump, see Fig. 6b. No broad WR emission is seen.

Again, we detect the presence of *nebular* He II 4686. The width of He II 4686 emission is comparable to that of [Fe III] and [Ar IV] , cf 0.6 ± 0.2 and 0.7 ± 0.1Å, respectively. The origin of this nebular He II 4686 emission is discussed in Section 7.

4   PROPERTIES OF THE KNOTS AND THEIR IONIZING CLUSTERS

In this section we derive the ages and extinction towards knots A and B and their ionizing clusters A1–4 and B1 using *stellar* (Section 4.1) and *nebular* (Section 4.2) diagnostics in the UV and optical respectively. Cluster sizes for A1–4, B1, C1 and C2 are also derived from the UV STIS image in Section 4.1.1. Note that no age or extinction estimates can be made for C1 and C2 since no spectroscopic data is available for these clusters.

4.1   UV derived cluster properties

4.1.1   Sizes

Cluster sizes were determined from the STIS UV image using the ISHAPE routine of Larsen (1999). The routine compares the observed cluster profile with PSF-convolved analytical functions that model the surface brightness of the clusters. The best-fitting function, determined by the χ^2 results, then gives the effective radii R_{eff}, or half light radius for each cluster. A correction for the true effective radii for elliptical profiles $R_{\mathrm{eff,ell}}$, as given by equation 11 of the ISHAPE user's guide, is made.

    We choose to model our clusters using King (1962) profiles for different concentration parameters c – where c is defined as the ratio of the tidal radius r_{t} to the core radius r_{c} and takes values of 15, 30 and 100 – and MOFFAT profiles for different power indices α, where α equals 1.5 or 2.5 (MOFFAT15 or MOFFAT25). Various fitting radii were used, ranging from a minimum radius that is set equal to the approximate size of the cluster to a maximum radius that is set to be the furthest one can move from the cluster without background contamination from a nearby source. The results of the models giving the most internally consistent FWHM and best χ^2 statistics are shown in Table 2. All the clusters appear to be very compact, with half light radii $\lesssim 3$ pc and sizes typical of SSCs (Larsen 2004).

4.1.2   Ages

We adopt the method of Chandar, Leitherer & Tremonti (2004) for determining the ages of our clusters by first correcting the STIS UV spectra for Galactic foreground extinction. We use the Seaton (1979) Galactic law for an E$(B\text{-}V)_{\mathrm{gal}} = 0.066$ mag (Schlegel, Finkbeiner & Davis 1998). We then normalise the spectra and compare them to the model data output of Starburst99 v5.0 (Leitherer et al. 1999) scaled from a 10^6 M$_\odot$ instantaneous burst with a 0.1–100 M$_\odot$ Kroupa (2001) IMF.

    Based on our abundance determinations made in Section 5.2, an LMC metallicity was assumed. UV O star spectra shortward of $\lambda \leqslant 1600$Å are taken from template stars in the Large and Small Magellanic Clouds
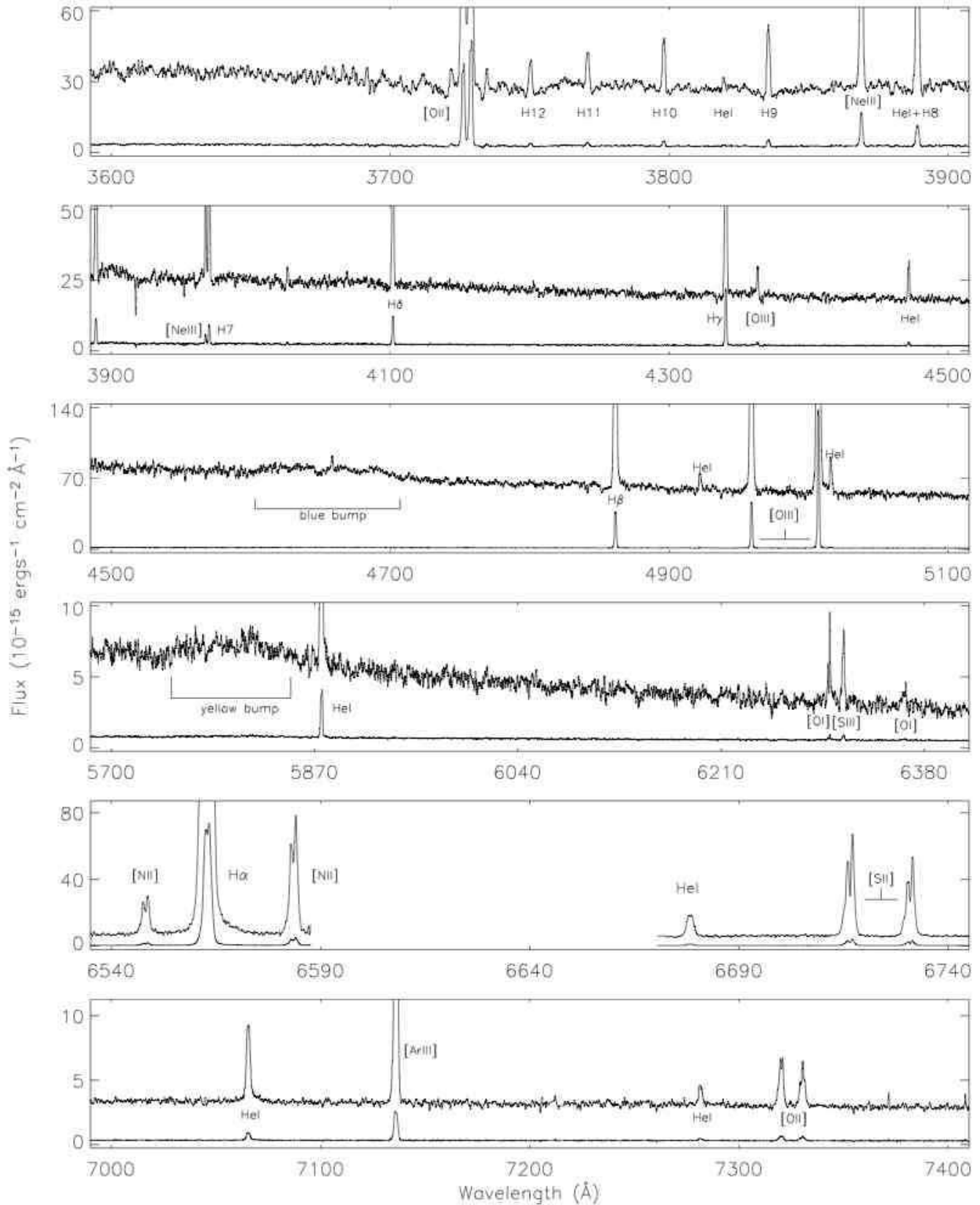
Figure 7. Velocity corrected UVES+VLT spectra of Tol 89-A covering the spectral range of 3600–7400 Å. In each panel the spectra are scaled to arbitrary flux values to show the detail in the spectra. The unscaled spectra are plotted to show the relative line intensities of the strongest emission lines. The velocity splitting in the strongest emission lines can be seen. The blue and yellow WR bumps are also indicated.
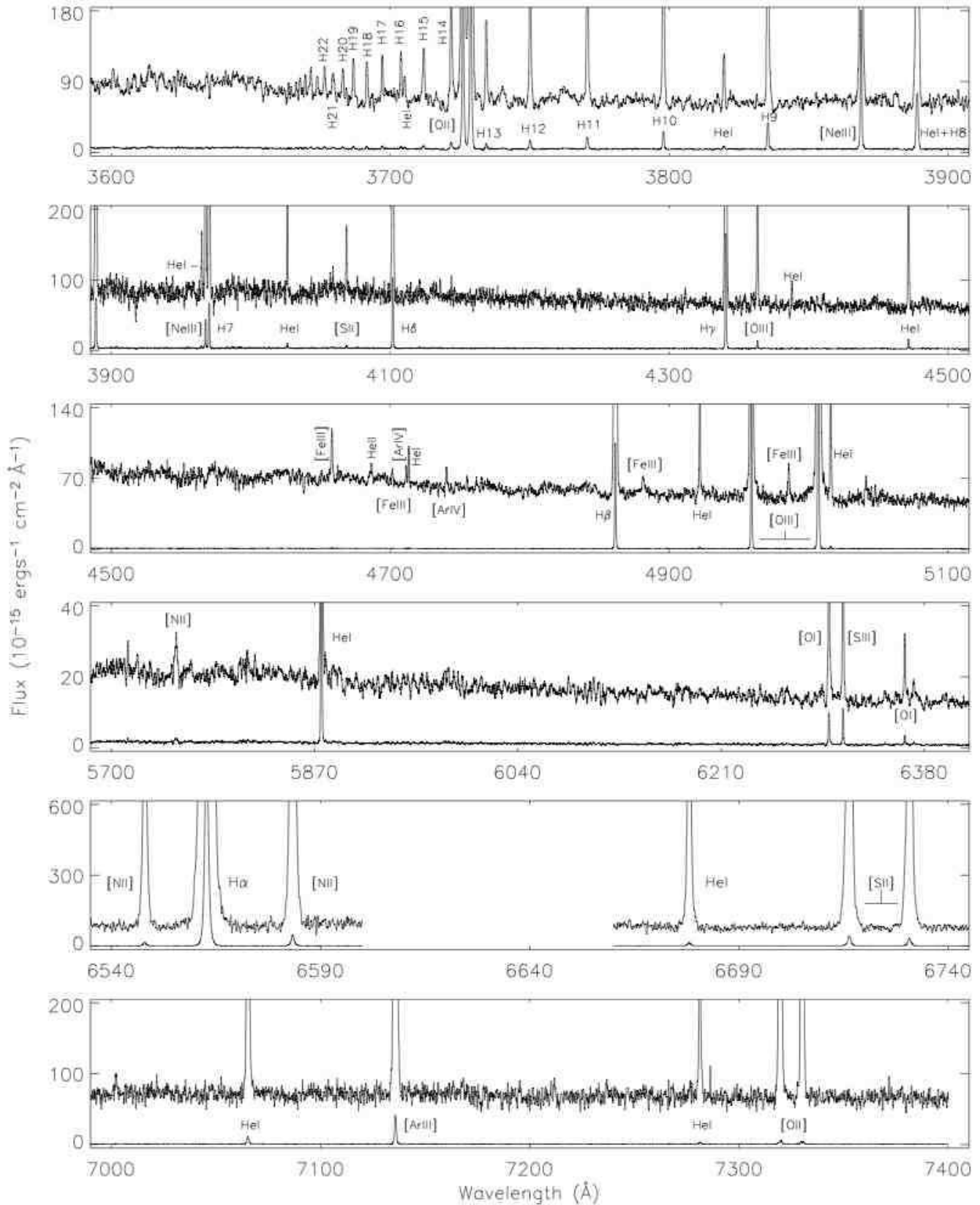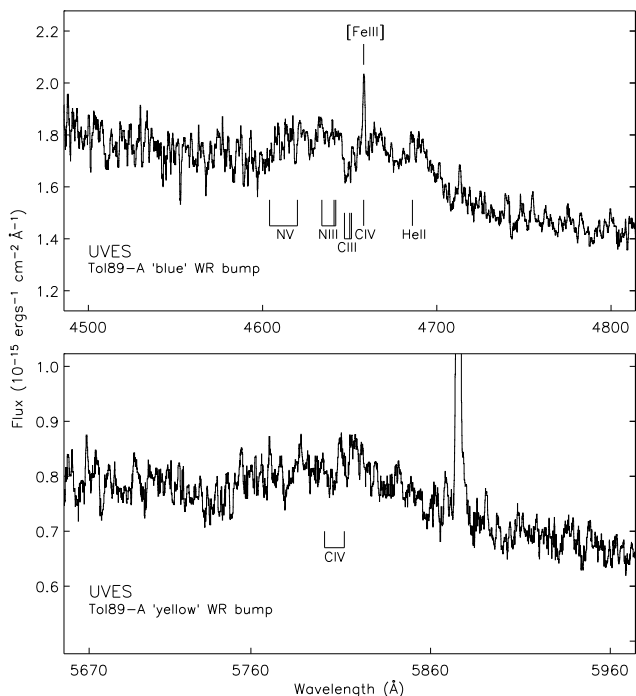
Figure 8. Velocity corrected UVES+VLT spectra of Tol 89-B covering the spectral range of 3600–7400 Å. In each panel the spectra are scaled to arbitrary flux values to show the detail in the spectra. The unscaled spectra are plotted to show the relative line intensities of the strongest emission lines.

Table 2. Results of the best-fitting analytical profiles giving the most internally consistent χ^2 statistics and FWHM for clusters A1–4, C1 and C2 seen in the UV STIS image. The FWHM and minor-to-major axis ratios are averages of between 4–6 measurements over different fitting radii.

Cluster	Model	FWHM (pix)	$\dfrac{\text{minor}}{\text{major}}$	R_{eff} (pix)	$R_{\text{eff,ell}}$ (pix)	$R_{\text{eff,ell}}$ ($''$)	$R_{\text{eff,ell}}$ (pc)
A1	MOFFAT 25	2.4	0.79	1.63	1.46	0.036	2.6
A2	King 15	2.4	0.73	1.69	1.46	0.036	2.6
A3	MOFFAT 25	2.8	0.75	1.92	1.68	0.041	3.0
A4	King 15	1.0	0.76	1.05	0.92	0.023	1.6
C1	MOFFAT 25	2.5	0.51	1.67	1.26	0.031	2.2
C2	MOFFAT 25	2.0	0.71	1.37	1.17	0.029	2.1

Figure 9. Velocity corrected UVES+VLT spectra showing the blue (*top*) and yellow (*bottom*) WR bumps in Tol 89-A. The blue bump is a blend of *nebular* [Fe III] 4658 and *stellar* N v 4620 N III 4640, C III/C IV λ4650/58 and He II 4686 – indicating the presence of both early (WNE) and late-type (WNL) nitrogen rich Wolf–Rayet stars. The yellow bump is due to C IV emission from the strong stellar winds of WC4–5 stars.

(Leitherer et al. 2001). All other empirical data are from spectral types at solar metallicity, i.e. the atlases of Robert, Leitherer & Heckman (1993) for WR stars and de Mello, Leitherer & Heckman (2000) for B stars.

In Fig. 10 we show the best-fitting models for clusters A1 and A2. We can see in the case of A1 that we are able to reproduce well the strengths of the Si IV 1400 and C IV 1550 O-star P-Cygni profiles, enabling us to constrain the age to 4.5±0.5 Myr. For A2 we determine a similar age of 5±1 Myr. The uncertainty is larger since we rely solely on the fit to Si IV 1400. This is due to the fact that the Starburst99 models fail to reproduce the C IV 1550 feature, whose strength implies a significant contribution from WC stars in A2; unlike in A1 where the fit to C IV 1550 is excellent. The WR spectral synthesis in the UV is rudimentary because it relies

on solar metallicity spectra of a few WR stars. Until detailed WR spectral synthesis is available for the UV wavelength range, it is difficult to draw any quantitative conclusions on the WR content of regions A1 and A2 from Starburst99 modelling alone. Our derived ages for A1 and A2 are consistent with the 4±1 Myr determined by Chandar et al. (2004) for their extraction of Tol 89-1 (= our A1 + A2).

Our age estimates for A3, A4 and B1 are somewhat more uncertain given the poorer S/N of the spectra; we obtain approximate ages of 3.0–5.5 Myr for A3 and A4 and < 3 Myr for B1 from the model fits. The age estimate for A4 is especially uncertain, due to the weakness of Si IV, with mid-WN stars contributing to the C IV profile, such that Starburst99 modelling is inadequate. We suspect that A4 has an age of ~3 Myr, given its similarity to mid-WN stars observed in young massive clusters (Section 6.1.2).

Given the age of cluster A3 one would also expect WR stars to be present. Whilst WC stars do not appear to be present from the observed CIV 1550 profile, weak HeII 1640 from WN stars is not excluded given the observed low S/N for this region. The presence of WN stars in A4 is discussed in Section 7.

4.1.3 Extinction

From the best-fitting age models we determine an estimate for the internal reddening E(B-V)$_{\text{int}}$ towards each cluster by dereddening the Galactic foreground extinction-corrected cluster spectra to match the slope of the best fitting Starburst99 model. The fit is performed over the wavelength range of 1240–1600 Å and the models normalised to match the continuum either side of C IV 1550. We adopted the stellar LMC extinction law of Howarth (1983) to deredden our UV spectra in favour of the Calzetti et al. (2000) starburst obscuration law used by Chandar et al. (2004). The latter is more appropriate for unresolved star forming galaxies than for effective point sources, such as is the case for Tol 89–A1 and A2. Similar conclusions were reached for NGC 3125–A1 by Hadfield & Crowther (2006).

The following internal reddening values are obtained for A1 and A2 respectively: 0.09 ± 0.02 and 0.08 ± 0.02 mag. This is equivalent to ≈ 1.0 ± 0.2 and 0.9 ± 0.2 mags of internal extinction at λ1500 (A_{1500}) for the Howarth (1983) LMC reddening law. Although our reddening estimates are in agreement with the value of 0.08 mag obtained by Chandar et al., the extinction at λ1550 obtained here is approximately twice that obtained using the Calzetti et al.
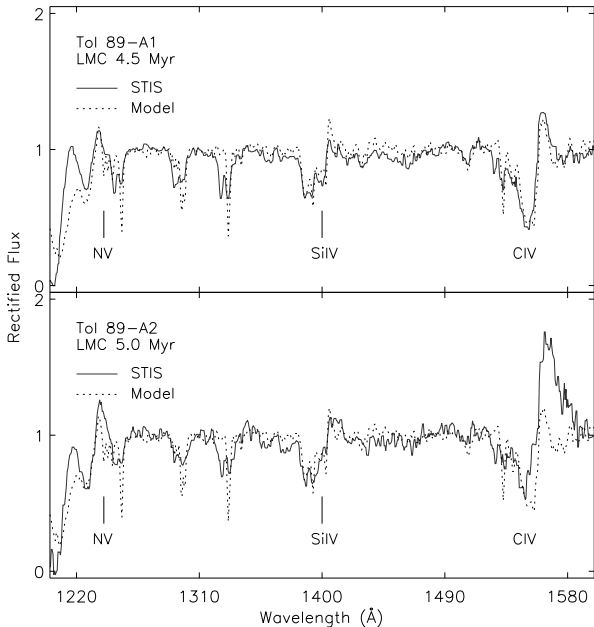
Figure 10. The rectified FUV spectra (*solid black line*) of clusters A1 (*top*) and A2 (*bottom*) shown with the best-fitting (age) Starburst99, LMC models (*dotted line*). The STIS spectra have been smoothed for clarity and velocity corrected.

starburst obscuration law; for which $A_{1500} = 0.4$ mag for $E(B\text{-}V)_{\rm int} = 0.08$ mag. For regions A3, A4 and B1 we obtain $E(B\text{-}V)_{\rm int}$ of 0.10 ± 0.03, 0.08 ± 0.03 and 0.17 ± 0.03 mag, or $A_{1500} \approx 1.1 \pm 0.3$, 0.9 ± 0.3 and 1.8 ± 0.3 mag respectively. Again, using the Calzetti et al. law the extinction at $\lambda 1500$ is approximately half that obtained using the LMC law (Howarth 1983).

4.2 Optically derived knot properties

4.2.1 Ages

Estimates for the ages of knots A and B were determined from the UVES spectra by comparing the equivalent widths of nebular Hβ emission to Starburst99 predictions. We obtain equivalent widths of 55 and 295 Å for A and B respectively. For an instantaneous burst of LMC metallicity and a 0.1–100 M$_\odot$ Kroupa IMF, this corresponds to ages of $\sim$4.5 and 2.5 Myr; assuming that all hydrogen ionising photons are absorbed within the HII region. Schaerer, Contini & Kunth (1999) determine an age of 4.5–5.0 Myr for Tol 89 by comparing their measured Hβ equivalent widths with standard, SMC population synthesis models.

The ages of the knots derived from the $EW(H\beta)$ are in excellent agreement with the cluster ages derived in Section 4.1.2. The average cluster age in knot A (A1–4) is $\approx 4.5 \pm 1.0$ Myr, which is in excellent agreement with the 4.5 Myr determined for Tol 89-A. An age < 3 Myr is derived for B1, which is also in good agreement with the < 2.5 Myr derived for Tol 89-B.

4.2.2 Extinction

In the optical, the total extinction $E(B\text{-}V)_{\rm tot}$[2] is determined from the Balmer line decrement. For both the STIS and UVES data we use only the Hα and Hβ line fluxes to determine the extinction for the following reasons. In the STIS data, the higher order Balmer lines of Hγ and Hδ are very weak and thus are not reliable indicators of $E(B\text{-}V)_{\rm tot}$. In the UVES data we observe little to no underlying stellar absorption. After correction for galactic foreground extinction we determine an internal reddening value for knot A which is consistent with there being zero reddening. The low extinction towards knot A is surprising given it's young age (~ 4.5 Myr) and suggests that clusters very quickly disperse their natal clouds within a few Myr. For knot B, we obtain an internal reddening value $E(B\text{-}V)_{\rm int}$ of ~ 0.24 from both the STIS and the VLT spectra. We therefore adopt the following (total) reddening values for knots A and B of 0.07 ± 0.01 and 0.29 ± 0.03 mag respectively. Previous determinations of the average reddening over the Tol 89 complex lie within the bounds of our estimates, cf 0.12 (Terlevich et al. 1991: $C(H\beta) = 0.18$) and 0.20 (Durret et al. 1985).

5 NEBULAR PROPERTIES OF THE KNOTS

Line fluxes and equivalent widths for nebular lines were determined using the ELF (emission line fitting) and EW (equivalent width) routines within the STARLINK package DIPSO. Fluxes were measured by Gaussian fitting, allowing for line centres and widths to vary freely – except when fitting doublets, in which case widths and relative line centres were constrained. The observed and intrinsic line fluxes normalised to H$\beta = 100$ are listed in Table 3.

We find that the strongest nebular emission lines are composed of a narrow and a broad component, both centred at similar velocities. In addition for knot A, we detect line splitting in the narrow component with a separation between the blue (V1) and red (V2) components of 48 ± 1 km s^{-1}. The FWHMs of the broad and narrow components are for knot A: 111 ± 2, 32 ± 2 (blue component), 41 ± 2 km s^{-1} (red component), and 71 ± 2, 27 ± 2 km s^{-1} for knot B. The multiple components are seen in the following emission lines: Hα, Hβ, [O II] $\lambda\lambda 3726/29$, $\lambda\lambda 7319/30$, [O III] $\lambda\lambda 4959, 5007$, [N II] $\lambda\lambda 6548/84$, and [S II] $\lambda\lambda 6717/31$. In lines with poorer S/N no broad or velocity-split components are detected.
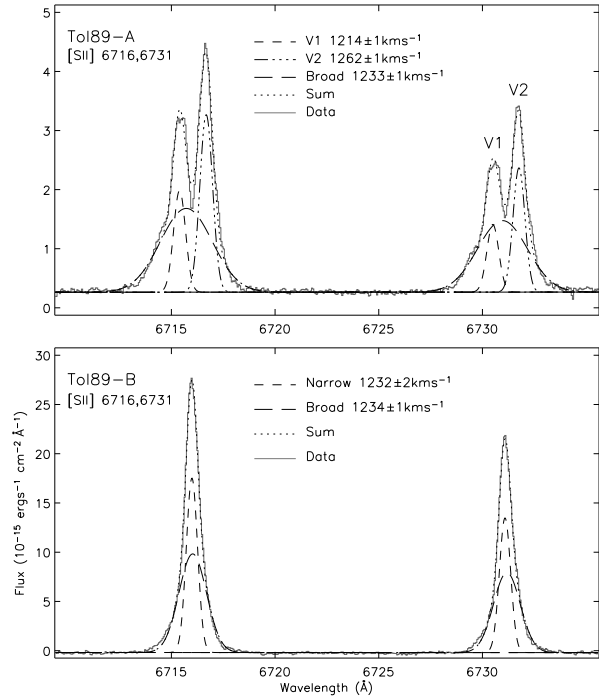
In Fig. 11 we show, as an example, the [S II] $\lambda\lambda 6716/31$ emission seen in A (*top*) and B (*bottom*) with the best-fitting Gaussians superimposed. The broad components account for a significant fraction of the total line flux (31 and 50 per cent for A and B respectively). The broad components are symmetrical with respect to the mean velocities of the narrow components and have the same central velocities for both A and B, suggesting a common origin. The only apparent difference between the broad components in the A and B spectra is in the line width (111 vs. 71 km s^{-1}).

Mean heliocentric radial velocities for A and B were determined by averaging the velocities of all the Gaussian

---

[2] Here we define $E(B\text{-}V)_{\rm tot}$ to be the Galactic foreground contribution $E(B\text{-}V)_{\rm gal}$ (0.066 mag; Schlegel et al. 1998) plus the internal contribution, $E(B\text{-}V)_{\rm int}$.

Table 3. Observed (F_λ) and intrinsic (I_λ) nebular line fluxes for knots A and B relative to $H\beta = 100$, and equivalent widths, W_λ, of WR emission lines seen in knot A. No WR emissions are detected in knot B.

λ_0	Ion	A		B	
		F_λ	I_λ	F_λ	I_λ
Nebular Emission Lines					
3726	[O II]	73.92	78.23	39.34	50.46
3729	[O II]	101.20	107.10	51.43	65.93
3869	[Ne III]	26.33	27.70	27.95	34.95
3967	[Ne III]	6.63	6.94	7.25	8.90
4026	He I	1.81	1.90	1.50	1.81
4069	[S II]	0.74	0.77	0.71	0.85
4076	[S II]	...	...	0.18	0.21
4102	Hδ	22.49	23.41	22.08	26.34
4121	He I	...	...	0.18	0.22
4144	He I	...	...	0.18	0.21
4341	Hγ	48.87	50.25	41.84	47.31
4363	[O III]	2.28	2.34	2.60	2.92
4471	He I	3.22	3.29	3.40	3.73
4658	[Fe III]	0.68	0.68	0.57	0.60
4686	He II	...	...	0.12	0.12
4702	[Fe III]	...	...	0.10	0.10
4711	[Ar IV]	0.50	0.51	0.22	0.23
4713	He I	...	...	0.45	0.46
4740	[Ar IV]	0.32	0.33	0.24	0.25
4959	[O III]	121.40	120.80	166.40	162.50
5007	[O III]	363.20	360.30	498.50	481.50
5016	He I	2.18	2.16	2.06	1.99
5048	He I	...	...	0.11	0.10
5518	[Cl III]	0.52	0.50	0.49	0.42
5538	[Cl III]	0.41	0.39	0.31	0.26
5755	[N II]	...	...	0.46	0.38
5876	He I	11.60	11.07	15.07	12.24
6300	[O I]	1.85	1.74	1.71	1.30
6312	[S III]	1.42	1.33	2.02	1.54
6364	[O I]	0.22	0.21	0.53	0.40
6548	[N II]	4.53	4.23	5.42	3.98
6563	Hα	290.20	270.40	390.50	286.30
6583	[N II]	14.91	13.88	17.26	12.62
6678	He I	3.09	2.87	4.80	3.47
6716	[S II]	13.29	12.33	16.31	11.71
6731	[S II]	9.97	9.24	12.80	9.18
7065	He I	2.44	2.24	4.29	2.95
7136	[Ar III]	8.99	8.24	16.24	11.06
7281	He I	0.52	0.47	0.91	0.61
7319	[O II]	1.56	1.42	0.79	0.52
7331	[O II]	0.84	0.76	1.19	0.79
9069	[S III]	27.70	24.35	56.23	31.90
9531	[S III]	97.78	85.32	199.60	109.70
log Hβ		−13.32	−13.23	−12.86	−12.43
E(B-V)$_{\rm tot}$		0.07		0.29	
Broad WR Emission Lines in Region A					
		I_λ (10^{-15}ergs s^{-1})		W_λ (Å)	
N V λ4606, 4619		3.6±0.6		2.2±0.4	
N III λ4634−41		2.1±0.6		1.2±0.4	
C III / C IV λ4650/58		3.4±0.4		2.1±0.2	
He II λ4686		3.9±0.4		2.6±0.3	
C IV λ5808		5.9±1.4		11.8±0.7	

Figure 11. UVES spectra of knots A (*top*) and B (*bottom*) in the spectral range of the [S II] 6716, 6731 doublet showing the multiple Gaussian component fits to the line profiles. The broad (*long–dash*), narrow (*short–dash*) and summed components (*dotted line*) are plotted. In region A, the two narrow velocity components, V1 (*short–dashed*) and V2 (*dash–dot–dot–dot line*) can be seen. The central velocities of the Gaussian fits are given in each plot.

components (broad and narrow) fit to the emission lines in each region and are found to be 1241±2 and 1234±2 km s^{-1} respectively. These results are consistent with the values reported in the literature: 1232 ± 51 (Durret et al. 1985) and 1226 ± 11 km s^{-1} (Schaerer et al. 1999).

Overall, we find that knots A and B have similar velocities, differing by 7 km s^{-1}, and thus are part of the same star-forming complex. For A, we see velocity splitting, suggesting that the winds from the clusters have swept up the surrounding interstellar gas into a shell which is currently expanding at 24 km s^{-1}. For B, we see no line splitting which is in accord with its younger age. We also detect a broad component which appears to be common to both regions A and B. The maximum width of these features corresponding to the full width at zero intensity (FWZI) is 1140 and 940 km s^{-1} for A and B; this suggests that the two knots contain gas with velocities up to ∼ 450–600 km s^{-1}. We consider the origin of this high velocity component in Sect. 7.

5.1 Electron densities and temperatures

Electron densities N_e, and temperatures T_e, were determined using the diagnostic line ratios listed in Table 4. The individual *broad* and *narrow* velocity components were summed in our calculation of N_e and T_e due to the fact that no broad or velocity shifted components were detected for the weaker, poorer S/N, temperature-sensitive diagnostic lines ($\lambda\lambda$4069, 4076, 4363 and 5755). We note that the ratios

of the line fluxes for the broad and narrow components in [S II] are identical (see Fig. 11) suggesting that they have similar electron densities.

Electron densities were calculated assuming a constant T_e of 10 000 K. Since [O II] and [S II] give consistent N_e (see Table 4) we take the average of the two to be representative of the densities in Tol 89-A and B. We find N_e of $\approx 90 \pm 40$ and $\approx 150 \pm 40$ cm^{-3} respectively. [Ar IV] and [Cl III] probe denser regions of gas and thus give higher N_e estimates. Refined estimates for the electron temperatures were then determined using the average N_e determined from O$^+$ and S$^+$ above. Using the most consistent T_e between the different diagnostic line ratios, we derive the following 'average' T_e of $\approx 10\,000 \pm 300$ K for A; neglecting $T(S^+)$ due to its large uncertainty.

For region B we derive a value of $9\,800 \pm 300$ K. We exclude the large T_e derived from N$^+$ and O$^+$ because in moderate to high-excitation HII regions the [N II] 5755 and [O II] 7330 lines can be excited by the recombination of N^{2+} and O^{2+} in the higher-excitations zones (Rubin 1986; Liu et al. 2000), thus leading to higher electron temperatures (see Table 4).

5.2 Abundances

Ionic abundances were calculated using the average N_e and T_e determined in Section 5.1 (see Table 4). To determine total abundances we adopt the following expressions given by Eqn. 1; where the ionisation correction factors (ICF) for N, S and Ar are as defined in equations 15, 18 and 19, respectively, of Izotov, Thuan & Lipovetsky (1994).

$$\frac{O}{H} = \frac{O^+ + O^{2+}}{H^+}$$

$$\frac{S}{H} = ICF(S)\frac{S^+ + S^{2+}}{H^+}$$

$$\frac{N}{H} = ICF(N)\frac{N^+}{H^+}$$

$$\frac{Ar}{H} = ICF(Ar)\frac{Ar^{2+} + Ar^{3+}}{H^+}$$

$$(1)$$

We derive 12+log(O/H) for knots A and B respectively of 8.27 and 8.38 which are in good agreement with the value of 8.32 derived by Schaerer et al. (1999); while Durret et al. (1985) derive a much lower oxygen content of 8.03. Oxygen and sulphur abundances are very similar to those of the LMC (Russell & Dopita 1990), such that hereafter we assume an LMC metallicity for Tol 89, although nitrogen and argon abundances are somewhat lower. With respect to 30 Dor (Peimbert 2003), knots A and B are moderately depleted by 0.25–0.5 dex.

6 MASSIVE STAR POPULATION

In the following section we examine the massive star population in Tol 89, applying both empirical and synthesis techniques in the optical and the UV.

Table 4. Derived physical properties and abundances from the UVES spectra of Tol 89 for knots A and B. A comparison is made with the abundances derived for the LMC (Russell & Dopita 1990) and 30 Dor (Peimbert 2003).

Diagnostic Line Ratio	Knot A	Knot B	LMC[a]	30 Dor[b]
Density	$N_e(\mathrm{cm}^{-3})$			
[O II] $\lambda3726/\lambda3729$	90^{+40}_{-50}	140 ± 30		
[S II] $\lambda6731/\lambda6716$	100 ± 30	150 ± 50		
[Ar IV] $\lambda4740/\lambda4711$	...	4300^{+2000}_{-1800}		
[Cl III] $\lambda5537/\lambda5517$	510–1450	...		
Temperature	$T_e(\mathrm{K})$			
[N II] $\lambda5755/\lambda6584$	...	14800 ± 400		
[O II] $\lambda7330/\lambda3726$	9900 ± 200	13100 ± 400		
[S II] $\lambda4068/\lambda6717$	9400 ± 900	10000 ± 500		
[O III] $\lambda4363/\lambda5007$	10000 ± 500	9800 ± 100		
[S III] $\lambda6312/\lambda9069$	10000 ± 200	9500 ± 100		
Average				
$N_e(\mathrm{cm}^{-3})$	90 ± 40	150 ± 40		
$T_e(\mathrm{K})$	10000 ± 300	9800 ± 300		
Abundances				
O$^+$/H$^+$(x10^4)	0.68 ± 0.09	0.49 ± 0.06		
O^{2+}/H$^+$(x10^4)	1.21 ± 0.17	1.91 ± 0.17		
O/H(x10^4)	1.88 ± 0.36	2.40 ± 0.35		
12+log(O/H)	$8.27^{+0.08}_{-0.09}$	$8.38^{+0.06}_{-0.07}$	8.37	8.50 ± 0.02
S$^+$/H$^+$(x10^6)	0.46 ± 0.03	0.51 ± 0.04		
S^{2+}/H$^+$(x10^6)	2.94 ± 0.15	4.23 ± 0.23		
ICF(S)	1.28	1.57		
S/H(x10^6)	4.37 ± 0.36	7.47 ± 0.66		
12+log(S/H)	$6.74^{+0.03}_{-0.04}$	6.87 ± 0.04	6.87	6.99 ± 0.10
N$^+$/H$^+$(x10^6)	1.97 ± 0.13	2.10 ± 0.15		
ICF(N)	2.78	4.92		
N/H(x10^6)	5.47 ± 0.37	10.30 ± 0.73		
12+log(N/H)	6.74 ± 0.03	7.01 ± 0.03	7.07	7.21 ± 0.08
Ar^{2+}/H$^+$(x10^7)	7.19 ± 0.36	6.67 ± 0.51		
Ar^{3+}/H$^+$(x10^7)	0.63 ± 0.11	0.56 ± 0.07		
ICF(Ar)	1.14	1.04		
Ar/H(x10^7)	8.91 ± 1.46	7.52 ± 1.02		
12+log(Ar/H)	$5.95^{+0.07}_{-0.09}$	$5.88^{+0.06}_{-0.07}$	6.07	6.26 ± 0.10

[a] Values taken from Russell & Dopita (1990).
[b] Values taken from Peimbert (2003) adopting $t^2 = 0.033$.

6.1 Empirical technique: line luminosities

6.1.1 Determining the dominant WR subtypes

Empirically, the WR population is estimated from average line luminosities of WR stars and is thus dependent on the dominant subtypes assumed to be present (Schaerer & Vacca 1998).

For WN stars we use the line width of He II 1640 in the UV as the main discriminator of subtype, since it can be attributed almost entirely to WN stars; in optical low resolution data, $\lambda4686$ is blended with nebular emission lines ([Fe III] and [Ar IV]) or with other WN *and* WC line components (e.g. N III 4634–41 and C III /C IV $\lambda4650/58$). Using the generic LMC UV spectra presented in
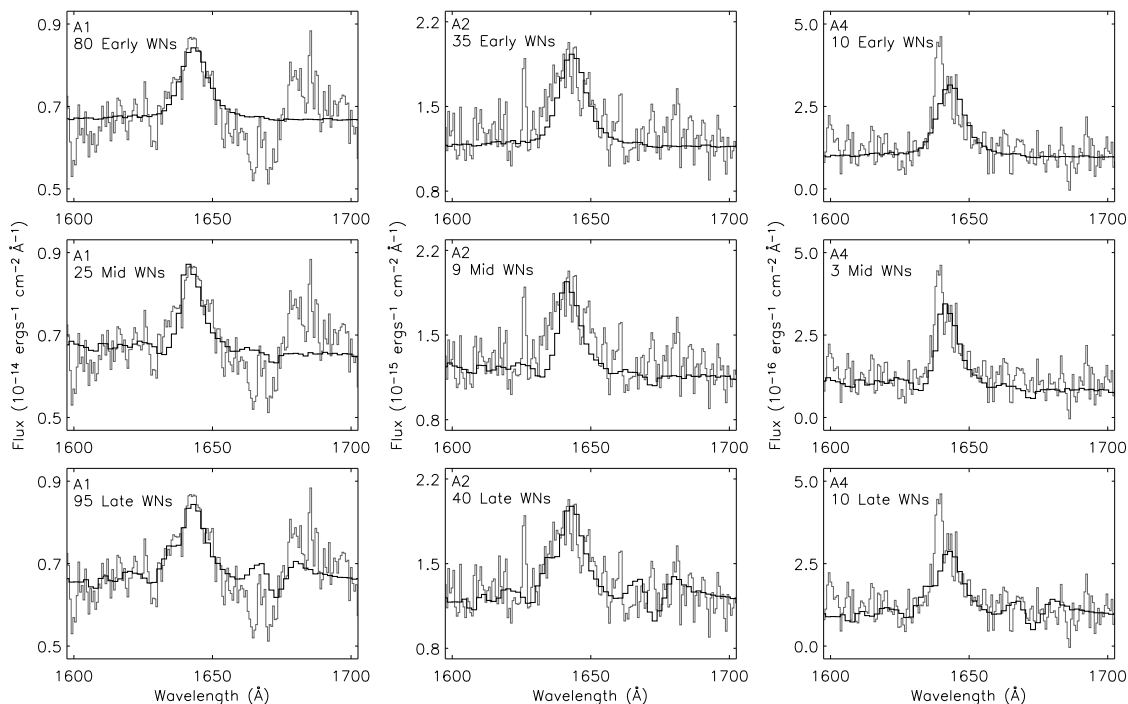
Figure 12. Plots showing the fits to He II 1640 for clusters A1 (*left panel*), A2 (*centre panel*) and A4 (*right panel*) using the generic LMC UV spectra presented in Crowther & Hadfield (2006) of early (*top*), mid (*middle*) and late-type (*bottom*) WNs.

Crowther & Hadfield (2006; hereafter CH06) of early, mid and late WNs we reproduce the line morphology of He II 1640 in A1, A2 and A4 (see Section 6.1.2).

In Fig. 12 we show the fits obtained to He II 1640. The apparently good fit from the late-type templates is due to the poorer resolution of the template spectra in which the apparent He II 1640 line width is due to blending with Fe IV 1632. A dominant late-type population can be excluded since λ1632, if present, would be separated from λ1640 at the resolution of the STIS UV spectra (3.1 Å). Although a dominant population of mid-type WNs cannot be ruled out entirely, the width of the template line profile is narrower than observed in either A1 or A2. We therefore conclude that the dominant WN population in A1 and A2 is early-type from the fit to He II 1640[3]. For cluster A4 an excellent fit to the He II 1640 line profile is obtained using the mid-type templates (see *middle right panel* of Fig. 12) and we therefore conclude that WN5–6 stars dominate in A4.

In contrast, for WC stars we use the optical wavelength regime to determine the main subtype because C IV 5808 can be attributed solely to WC stars, whilst C IV 1550 suffers from contamination by O and WN stars. From the presence of λ5808, and the absence of C III 5696 emission, we conclude that WC4–5 stars are the dominant subtype. This is supported by comparisons of our measurement of the FWHM of the λ5808 feature ($\sim 80 \pm 10$ Å) with those made by Crowther et al. (1998). We also infer that WC stars are solely present in cluster A2 from the strength of C IV 1550 relative to He II 1640 in the ultraviolet. *In summary, we as-sume that early WN (WN2–4) and WC (WC4) stars dom-inate the WR populations of A1 and A2, with WC4 stars absent in A1, while in A4 we assume that mid WN(WN5–6) stars dominate.*

6.1.2 Estimating the number of WR stars

UV: We estimate the WR populations of A1, A2 and A4 by scaling the generic LMC UV spectra presented in CH06 to match the intrinsic line morphologies of He II 1640 and C IV 1550, as shown in Figs. 12 and 13. A comparison of this technique versus simple line flux measurements is given in CH06.

For cluster A1 we estimate an early WN content of 80 stars, with WC stars absent. For A2, we estimate the WR content by simultaneously fitting C IV 1550 and He II 1640 until the strength of He II 1640 is reproduced, although we anticipate under-predicting C IV 1550 emission since O stars will also contribute to this line (recall Fig. 10). We esti-mate 10 early WN stars plus $\sim$25 early WC stars in A2. Remarkably, in cluster A4 we have been able to detect just three mid WN stars despite the large distance of 14.7 Mpc to Tol 89, which is testament to the dominance of WR stars in integrated (cluster/galaxy) spectra at UV wavelengths. To permit direct comparisons with the WR populations in-ferred from the optical UVES spectra of knot A, we sum the individual WR numbers in A1 and A2, as indicated in Table 5; we do not include the three WN5–6 stars derived for cluster A4 since these will not contribute significantly to the optical blue bump which we attribute entirely to WN2–4 stars.

Previously, Chandar et al. (2004) derive a value of 95 ± 68 late-type WN stars based on the their de-reddened

[3] A significant contribution to the He II 1640 emission line flux in A2 comes from WC stars and thus the width of λ1640 is less reliable as a discriminator of subtype in this case.

Table 5. WR content of Tol 89-A derived using the average LMC template WR spectra and line luminosities (erg s^{-1}) of Crowther & Hadfield (2006).

|	Diagnostic Line	Line Luminosity	A1	A2	A4	A
		Optical				
N(WN2–4)	$\lambda 4686$	8.4×10^{35}	...	...	...	100
N(WC4)	$\lambda 5808$	3.3×10^{36}	...	...	...	45
N(WR)			...	...	...	145
N(WC)/N(WN)			...	...	...	0.5
		UV				
N(WN2–4)	$\lambda 1640$	8.4×10^{36}	80	10	...	90
N(WN5–6)	$\lambda 1640$	1.7×10^{37}	...	...	3	3
N(WC4)	$\lambda 1550$	2.0×10^{37}	...	25	...	25
N(WR)			80	35	3	118
N(WC)/N(WN)			...	2.5	...	0.3

He II 1640 line flux for Tol 89–1 (which includes our clusters A1 and A2) and on the average He II 1640 line luminosity of a WNL star taken from SV98 ($L_{1640} = 1.2 \times 10^{37}$ ergs s^{-1}). From the line luminosity of $\lambda 1640$ given in their table 3, this equates to ~ 130 early WN stars using the CH06 LMC line luminosity for WN2–4 stars, a factor of 1.3 times larger than our estimate of ~ 100. We have measured the observed He II line flux from the spectrum of Chandar et al. (2004), kindly made available to us by the author, and have measured an observed flux that is in agreement with the sum of the observed fluxes in A1 and A2. Using the LMC template spectra of CH06, we derive an early WN content of ~ 90 in agreement with the results obtained for the sum of A1 and A2. Thus, we attribute this difference in WN numbers (cf ~ 100 and 130) to the different choice of extinction laws and techniques adopted.

Optical: Applying the same techniques in the optical, we estimate the number of WR stars from fits to He II 4686 (WN+WC) and C IV 5808 (WC) seen in knot A. Recall, no broad WR emission features are detected in knot B. Since WC stars are known to contribute to the strength of $\lambda 4686$, we begin by first estimating the number of WC stars responsible for the yellow bump ($\lambda 5808$), so that their contribution to $\lambda 4686$ can first be taken into account.

The results of our optical fitting procedure are shown in Fig. 14. From the fit to C IV 5808 (*top panel, dashed line*) we estimate a population of 45 early WC stars (cf 25 from the UV). Although the early-type empirical fit does not give the best match to $\lambda 4686$, a dominant population of mid-type WNs can be ruled out from the absence of N IV 4058, while the UV excludes a late-type dominant population from the absence of Fe IV 1632 emission. Taking into account the 45 early WC stars determined from C IV 5808, we derive a population of 100 early-type WN stars, which is in good agreement with the results obtained from the UV (cf 90 WNE for A1+A2), as shown in Table 5.

In summary, our UV and optical WR diagnostics give consistent populations of WN stars, plus reasonable agreement for WC stars. For Tol 89-A (which encompasses A1–4), our derived WR content of ~ 95 WNE and ~ 35 WCE stars
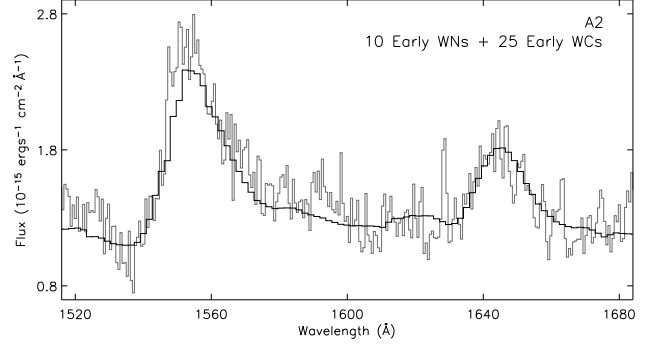
Figure 13. Plot showing the fit to C IV 1550 for cluster A2 using the generic LMC UV spectra presented in Crowther & Hadfield (2006) for a mixed population of early-type WN2–4 and WC4 stars.

indicates N(WC)/N(WN) ~ 0.4 (cf ~ 0.6; Schaerer et al. 1999).

6.1.3   Estimating the number of O stars

O-star numbers were derived following the methods outlined in Schaerer & Vacca 1998 (hereafter SV98) using the observed line luminosity of Hβ, which gives Q_0^{obs} – the total number of hydrogen ionising photons. Q_0^{obs} is then related to the total number of ionising O stars N(O) for a given subtype (typically O7V) using Eqn. 2; where the ionising contribution from a population of WR stars is taken into account:

$$N(O) = \frac{Q_0^{\mathrm{obs}} - N(WN)Q_0^{\mathrm{WN}} - N(WC)Q_0^{\mathrm{WC}}}{\eta_0(t)Q_0^{\mathrm{O7V}}}, \qquad (2)$$

and where Q_0^{O7V} is the Lyman continuum flux of an individual O7V star and $\eta_0(t)$ represents the IMF-averaged ionising Lyman continuum luminosity of a ZAMS population normalised to the output of one equivalent O7V star (Vacca 1994). N(WN) and N(WC) are the number of WN and WC stars respectively.

From the line luminosities of Hβ given in Table 6 we derive the following Q_0^{obs} values of ~ 320 and $\sim 2000 \times 10^{49}$ s^{-1} for knots A and B, respectively. The sum of these is ~ 3 times that obtained by Schaerer et al. (1999) who derived a Q_0^{obs} value of 708×10^{49} s^{-1} for the Tol 89 complex. This is likely due to the different choice in slit width ($1''\!.6$) and PA ($39°$) (cf Table 1).

Values of $\eta_0(t)$ are taken from the instantaneous burst models of SV98 (see their fig. 21) for the ages given by the equivalent width of Hβ obtained in Section 4.2.1. We adopt $\eta_0(t)$ values of 0.25 and 0.9 for knots A and B respectively (see Table 6). From a calibration of line blanketed Galactic O star models, $\log Q_0(\mathrm{O7V}) = 48.75$ s^{-1} (Martins et al. 2005). Recent studies of Magellanic Cloud O stars indicate ~ 2–4 kK higher temperatures than their Galactic counterparts (Massey et al. 2005; Heap et al. 2006). Consequently, we adopt $\log Q_0(\mathrm{O7V}) = 48.9$ s^{-1} at LMC metallicity (Hadfield & Crowther 2006). For typical LMC early WN and early WC star populations we adopt $\log Q_0$ values of 49.0 (Crowther & Smith 1996) and 49.4 (Crowther et al. 2002), respectively.
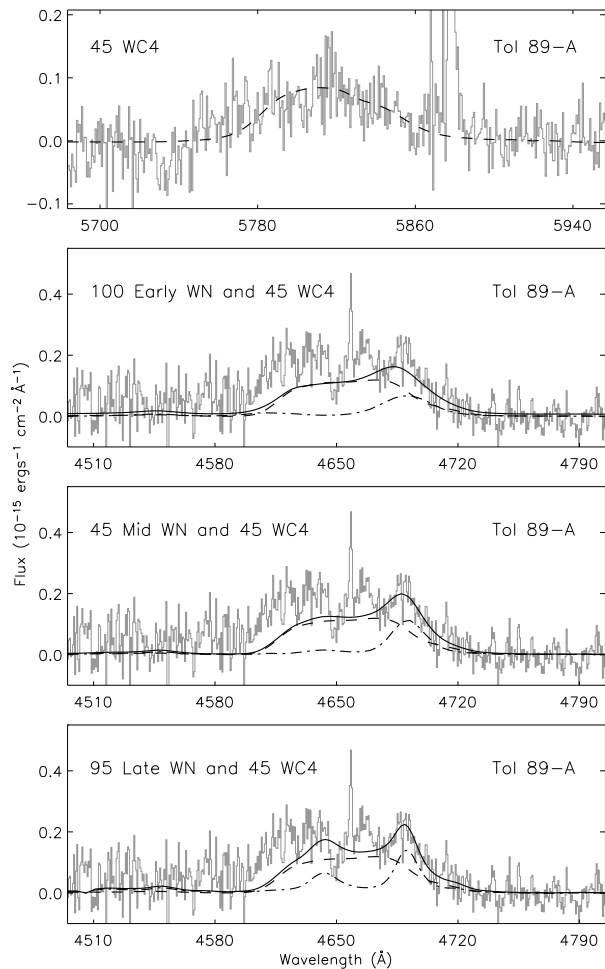
Figure 14. Plots showing the results of our line profile fitting. *Top:* Fit to the C IV 5808 feature using 45 LMC WC4 stars (*dashed line*). *2nd:* Plot showing the individual contributions from 100 early-type WNs (*dot-dashed line*) and 45 early type WCs (*dashed line*) to the blue bump. The sum of the individual components is shown as the *solid* line. *3rd:* As for *panel 2* but showing the individual contributions from 45 mid-type WNs (*dot-dashed line*). *Bottom:* As for *panel 2* but showing the individual contributions from 95 late-type WNs (*dot-dashed line*). The UVES spectra have been binned for clarity, continuum subtracted and velocity and extinction corrected.

For knot A we derive N(O)$\sim$ 690 from nebular Hβ emission, assuming a contribution from 95 WNE and 35 WCE stars giving N(WR)/N(O) $\sim$ 0.2 (see Table 6). For region B we derive a content of $\sim$ 2800 O stars from $Q_0^{obs} \sim 2000 \times 10^{49}\ s^{-1}$ and $\eta_0(t)$ determined from the SV98 models (see their fig. 21). This is about a factor two smaller than the value obtained by Johnson et al. using radio diagnostics ($\sim 3800 \times 10^{49} s^{-1}$, given a distance of 14.7 Mpc for $H_0 = 75$ km s^{-1}Mpc^{-1}; Schaerer et al.). We expect that the discrepancy between our derived value of Q_0^{obs} with that of Johnson et al. is due to the fact that radio observations probe deeper into the star-forming region, thus detecting massive stars that are otherwise obscured at optical wavelengths.

Table 6. Nebular derived O star content for Tol 89-A and B based on the line luminosity and equivalent width of Hβ: L(Hβ) and W(Hβ) respectively. The Hβ line fluxes (F$_\lambda$ and I$_\lambda$) are in units of ergs s^{-1} cm^{-2}. Line luminosities are derived based on D = 14.7 Mpc and are in units of ergs s^{-1}. The WR numbers for Tol 89-A are averages of UV and optical empirical calibrations from Table 5, whilst WR stars are not seen in Tol 89-B.

Region	A	B
F(Hβ)	4.7×10^{-14}	1.4×10^{-13}
I(Hβ)	5.9×10^{-14}	3.7×10^{-13}
L(Hβ)	1.5×10^{39}	9.5×10^{39}
$W(H\beta)$[Å]	55	295
Age (Myr)	4.5	2.5
Q_0^{obs}	3.2×10^{51}	2.0×10^{52}
Q_0^{O7V}	8.0×10^{48}	8.0×10^{48}
Q_0^{WN}	1.0×10^{49}	
Q_0^{WC}	2.5×10^{49}	
$\eta_0(t)$	0.25	0.9
N_{WN}	95	...
N_{WC}	35	...
N_O	685	2780
WR/O	0.2	...

6.2   Synthesis technique: Starburst99 modelling

In this section we compare the observed optical UVES spectrum of Tol 89-A and B to model predictions computed using the evolutionary synthesis code Starburst99 v5.0 (Leitherer et al. 1999). The code is an improved version of Starburst99, incorporating both a new set of evolutionary tracks from the Padova group for old and low-mass stars (Vázquez & Leitherer 2005), as well as a high-resolution (0.3 Å) optical spectral library (excluding WR stars) covering the full HRD (Martins et al. 2005).

We have implemented optical WR spectral line synthesis into Starburst99 by incorporating the high resolution (0.3 Å) *University College London* (UCL) grids of expanding, non-LTE, line-blanketed model atmospheres for WR stars (Smith, Norris & Crowther 2002). The UCL models have been calculated for the five metallicities represented in Starburst99 (0.05, 0.2, 0.4, 1 and 2 Z$_\odot$) using the CMFGEN code of Hillier & Miller (1998). The WR grids assume mass-loss scales with metallicity ($\dot{M} - Z$) and replace the pure helium, unblanketed, WR models of Schmutz et al. (1992). Hereafter, we refer to the computed models as the 'SB99+UCL' models.

6.2.1   Model parameters

Three models were calculated for an assumed 10^6 M$_\odot$ instantaneous burst between 0 and 8 Myr for a 0.1–100 M$_\odot$ Kroupa IMF. We choose to use the Geneva group solar and LMC metallicity stellar evolutionary tracks with enhanced mass-loss rates (Meynet et al. 1994). For the LMC metallicity tracks we use both the solar and LMC WR model atmospheres to test the effects of $\dot{M} - Z$ scaling (i.e. the default scaling with $\dot{M}$ is turned off). We adopt the Geneva evolutionary tracks over those of the Padova group (Girardi et al. 2000, and references therein) due to the better treatment of assigning WR atmospheric models to the evolutionary tracks (see Vázquez & Leitherer 2005).

6.2.2   Optical

The massive star content of Tol 89 is obtained by scaling the best-fitting SB99+UCL models to match the continuum flux of the dereddened spectrum over the wavelength range of 3000–7000 Å.

The observed spectrum is first corrected for foreground galactic extinction and the necessary amount of internal extinction is then applied to the observed data to match the slope of the best-fitting model, which is adjusted to match the optical continuum flux of the dereddened observed data. This scaling, along with the massive star content calculated by Starburst99 for our best-fitting (age) model, then gives the mass of the burst event, and thus the massive star population. The predicted N(WR)/N(O) and N(WC)/N(WN) number ratios calculated by Starburst99 are, of course, unchanged by this mass-scaling. The results of the fitting procedure are given in Table 7.

In Fig. 15 we show the best-fitting (age) SB99+UCL synthetic spectra to the blue bump in Tol 89-A for each of our models. The ages derived are slightly younger than the ~ 4.5 Myr derived in Section 4.2.1, cf 4.0 ± 0.5 (solar) and 3.5–4.0 Myr (LMC). We can see that the best-fitting model to the blue WR bump, and to He II 4686 in particular, is obtained for a 4 Myr solar model; although the solar model does not give the best fit to the overall continuum shape.

While the LMC models do give a better fit to the continuum, they fail to predict the strength of He II 4686, even with $\dot{M} - Z$ scaling for WR stars switched off. This result is not entirely unexpected since the initial mass for WR formation increases with decreasing metallicity (Meynet et al. 1994) and therefore we expect fewer WR stars to form for a given IMF. In neither of the models is the strength of N V 4620 matched, although all provide a good fit to C IV 5808. We note, however, that even the empirical LMC WR templates of CH06 fail to reproduce the observed profile of the blue bump (see Section 6.1).

We determine the mass of the burst in knot A to be in the range $(4\pm1) \times10^5$ M$_\odot$ (Solar) and 2–3 $\times10^5$ M$_\odot$ (LMC). Applying the same approach to knot B, we derive ages of less than 2.0 and 2.5 Myr, plus masses of 6 and 5 $\times10^5$M$_\odot$, for the Solar and LMC models, respectively. Using these masses, and the population predictions made by Starburst99, we derive the O and WR star numbers given in Table 7. Using the LMC models we derive N(O) = 660–910, N(WN) = 2–3 and N(WC) = 60–90 for Tol 89-A. The N(WR)/N(O) and N(WC)/N(WN) ratios are 0.1 and 17–35, respectively. The large N(WC)/N(WN) ratios predicted by Starburst99 are discussed in Section 7. For knot B we derive N(O) = 2030–2120 (Solar) or 1630–1740 (LMC) as shown in Table 7.

For Tol 89-A in particular, the O star numbers we derive from optical continuum fits with Starburst99 are in good agreement with the numbers indirectly derived from the nebular Hβ line luminosity in Section 6.1.3: cf $\sim$ 690 with $\sim$ 660–910 for Tol 89-A and $\sim$ 2800 with $\sim$ 1600–1700 for Tol 89-B for L(Hβ) versus Starburst99 modelling. In addition, the N(WR)/N(O) ratio inferred for Tol 89-A is also in excellent agreement, cf 0.2 versus 0.1–0.2, respectively.
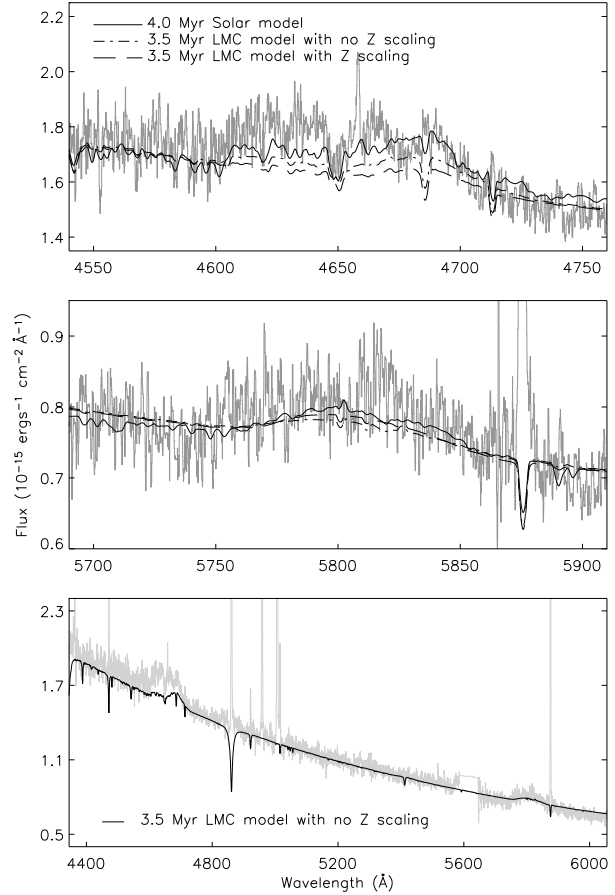
Figure 15. Plots showing the best fitting (age) SB99 + UCL models to the blue and yellow WR bumps of Tol 89-A for solar and LMC metallicities. A 3.5 Myr, $Z = 0.4Z_\odot$ metallicity instantaneous burst model for a 0.1–100 M$_\odot$ Kroupa IMF is shown over the spectral range 4400–6000 Å. The observed cluster spectrum has been velocity corrected and binned for clarity.

6.2.3   UV

We apply the same technique to the UV continuum, scaling the best-fitting (age) LMC Starburst99 models determined in Section 4.1.2 to match the flux levels of the dereddened cluster spectra of A1–4 and B1. We derive the following masses for A1 and A2 of $\sim$1–2$\times10^5$ and 2–6$\times10^4$ M$_\odot$, giving N(O) $\approx$ 310–680 and $\approx$ 40–190 respectively. For A3 and A4 we derive masses of 0.4–1.7$\times10^4$ and 1–5$\times10^3$ M$_\odot$, giving N(O) $\approx$ 10–60 and $\approx$ 5-20 respectively. The sum of the masses determined for A1–4 are consistent with the value derived from the optical, cf $\sim$1–3$\times10^5$ and $\sim$ 2–3$\times10^5$ M$_\odot$ respectively. Similarly, the O star numbers are also in good agreement: cf $\sim$ 660–910 and $\sim$ 370–950 from the optical and UV modelling respectively. These results are in excellent agreement with the $\sim$ 690 O stars derived from the nebular Hβ approach. For B1 we derive a mass of $\sim 3\times10^4$ M$_\odot$, giving N(O) $\approx$ 80–120. This mass is significantly smaller than the $\sim 5 \times 10^5$ M$_\odot$ derived from the optical UVES spectrum for Tol 89-B, which optical STIS imaging reveals is made up of at least 5 clusters (see leftmost inset of Fig. 2).

Table 7. Massive star content derived from SB99+UCL modelling of an instantaneous bursts with a Kroupa IMF ($\alpha = 1.3, 2.3$) and the following mass boundaries: 0.1 (M_{low}), 0.5 and 100 (M_{up}) M$_\odot$. LMC and Solar metallicity models are presented, in which O and WR populations result from optical continuum and emission line fits, respectively.

Model	LMC, Z= 0.4Z$_\odot$ UV					LMC, Z= 0.4Z$_\odot$ Optical		Solar Optical	
Region	A1	A2	A3	A4	B1	A	B	A	B
Age (Myr)	4.5±0.5	5.0±1.0	3.0–5.5	3.0–5.5	< 3.5	3.5–4.0	< 2.5	4.0 ± 0.5	< 2
Mass ($\times 10^5$ M$_\odot$)	1–2	0.2–0.6	0.04–0.17	0.01–0.05	0.3	2–3	5	4 ± 1	6
N(O)	310–680	40–190	10–60	5–20	80–120	660–910	1630–1740	670–1620	2030–2120
N(WN)	...	...	...	...	...	2–3	...	5–20	...
N(WC)	...	...	...	...	...	60–90	...	90–240	...
N(WR)/N(O)	...	...	...	...	...	0.1	...	∼ 0.2	...
N(WC)/N(WN)	...	...	...	...	...	17–35	...	7–31	...

7 DISCUSSION

7.1 Tol 89 as a GHR

Tol 89 is conspicuous by being the only large site of star formation in NGC 5398. Johnson et al. (2003) note that Tol 89 is among the most luminous radio H II regions yet observed and is comparable to NGC 5471 in M 101.

Tol 89 is composed of three knots of star formation which we denote as A, B and C. Optical HST/STIS imaging resolves the two brightest optical knots of star formation (A and B) into multiple clusters. Each is a massive burst of star formation in its own right, having produced multiple young compact massive clusters (R$_{\text{eff}}$ ⩽ 3 pc, M >∼ $10^{3–5}$ M$_\odot$) over very short time scales (∼ few Myr). The brightest cluster in knot A (A1), for example, has a mass of ∼1–2×10^5 M$_\odot$, while a total mass of ∼ 6×10^5 is inferred for the ionizing sources at the heart of Tol 89-B. A further two young compact (R$_{\text{eff}}$ ∼ 2 pc) massive clusters C1 and C2 are identified in the STIS UV image. The presence of so many young compact massive clusters within such an isolated GHR makes Tol 89 a rather unusual object. Typical GHRs in non-interacting, late-type spiral galaxies tend to host groupings of fewer and less massive (∼ $10^{3–4}$ M$_\odot$) clusters (e.g. NGCs 5461, 5462 and 5471 in M 101; Chen et al. 2005, and NGCs 592, 595 and 588 in M 33; Pellerin 2006) or multiple OB associations (e.g. NGC 604 in M 33; Hunter et al. 1996).

The fact that Tol 89 is located at the end of the bar in NGC 5398 indicates it may have been formed through gas inflow in a high pressure environment – the conditions under which SSCs are thought to form (Elmegreen & Efremov 1997). However, Johnson et al. (2003) suggest that the weak bars found in late-type galaxies are not strong enough to generate the required gas inflow. It is therefore not clear why so many young compact massive clusters have formed in Tol 89.

Larsen & Richtler (1999, 2000) have shown that massive star clusters do form in normal galaxies which show no obvious signs of recent interaction – *although these typically form in isolation*. They find that the formation of young massive clusters is favoured in environments with active star formation and thus suggest that their formation in starbursts or mergers may simply be extreme cases of a more general phenomenon. One possible explanation for the presence of such a massive star forming region is that the parent galaxy NGC 5398 may be undergoing some form of

interaction. A detailed investigation of NGC 5398 and its environment is needed to settle this issue.

In Table 8 we compare the properties of Tol 89 with the three GHRs in M 101 and 30 Doradus in the LMC. It can be seen that Tol 89 is comparable to, but no more exceptional than, the GHRs presented in Table 8 in terms of its Hα/radio luminosities and size. The area normalised star formation rate (SFR) of Tol 89 is ≈ 0.1 M$_\odot$ yr^{-1} kpc^{-2} and is comparable to the values derived for the cluster complexes in M 51 (see table 1 of Bastian et al. 2005) and to the definition of a starburst galaxy (0.1 M$_\odot$ yr^{-1} kpc^{-2} Kennicutt et al. 2005). The SFR rates in Table 8[4] are derived using the prescription of Kennicutt (1998): Σ_{SFR} (M$_\odot$ yr^{-1}) $= 7.9 \times 10^{-42} L_{\text{H}\alpha}$ (ergs s^{-1}).

7.2 Nebular emission lines

We first consider the origin of the nebular He II 4686 emission in Tol 89–B. This detection is to our knowledge the first in a WR galaxy with a metallicity greater than 0.2 Z$_\odot$ (cf. Guseva, Izotov & Thuan 2000). The detection in Tol89-A is somewhat ambiguous – due to the poor quality of the observations – nevertheless, nebular He II 4686 is expected to originate from weak-lined, metal-poor early-type WN or WC stars (Smith et al. 2002). As for Tol 89-B, the absence of WR stars implies that either the most massive O stars are responsible for providing the He II ionizing photons, or that other (non-photoionizing) mechanisms such as collisional shocks may be responsible for this emission.

The intrinsic flux ratio relative to Hβ, $I(\lambda 4686)/I(H\beta)$, is ≈ 1×10^{-3}. Schaerer & Vacca note that for young bursts dominated by O stars ($t < 3$ Myr), typical values for $I(\text{He II } 4686)/I(H\beta)$ lie between 5×10^{-4} and 2×10^{-3} (see their fig. 8). Thus, it would seem that our $I(\text{He II } 4686)/I(H\beta)$ ratio is approximately consistent with

---

[4] The value for Tol 89 is derived from the Hα flux estimated from the Hα images obtained as part of the *Spitzer Infrared Nearby Galaxies Survey* (SINGS) Legacy Project (Kennicutt et al. 2003). The observations were carried out at the Kitt Peak National Observatory (KPNO) 2.1 m telescope. We note that this value is derived from the observed (i.e. non-extinction corrected) Hα emission flux in accordance with the results presented by Chen et al. (2005) in their table 1.

Table 8. Comparison of Tol 89 with NGCs 5461, 5462 and 5471 in M 101 and 30 Doradus in the LMC. Values for Tol 89 are derived from Hα images obtained as part of the SINGS Legacy Project (Kennicutt et al. 2003). The observations were carried out at the Kitt Peak National Observatory (KPNO) 2.1 m telescope. L_{6cm} for Tol 89 comes from Johnson et al. (2003). Values for the three GHRs in M 101 and 30 Dor in the LMC are taken from table 1 of Chen et al. (2005), except the star formation rates (SFR) which were calculated using the prescription of Kennicutt (1998). The $L_{H\alpha}$ are not extinction corrected for any the GHRs presented in the table.

GHR	Tol 89	NGC 5461	NGC 5462	NGC 5471	30 Dor
Angular Size ($''$)	24×18	40×25	48×33	17×17	1200×1200
Linear Size (pc)	1700×1230	1400×875	1680×1150	600×600	290×290
$L_{H\alpha}$ (ergs s^{-1})	1.9×10^{40}	2.7×10^{40}	1.3×10^{40}	2.2×10^{40}	3.9×10^{39}
SFR$_{H\alpha}$ (M$_\odot$ yr^{-1} kpc^{-2})	0.07	0.17	0.03	0.47	0.36
L_{6cm}	6.2×10^{26}	1.4×10^{27}	9.1×10^{26}	7.4×10^{26}	...

a young starburst event in the pre-WR phase (in agreement with the fact the we do not detect any WR emissions). However, the SNC02 models – which include a more thorough treatment of chemistry and line blanketing in their WR models – predict $I(\lambda 4686)/I(H\beta)$ ratios that are a factor of ≈ 10 lower for all ages ($\sim 10^{-5}$ and $\sim 10^{-4}$), in which the lowest metallicity models predict the hardest ionizing flux distributions. During the pre-WR phase the SV98 and SNC02 models differ due to the use of the COSTAR (SV98) and WM-Basic (SNC02) models (see Smith et al. 2002, for details).

Consequently, one does not anticipate nebular He II 4686 in young starburst regions, such as Tol 89-B, to arise from O stars. Garnett et al. (1991) discuss H II regions in which nebular He II 4686 is observed. In most cases, Wolf-Rayet stars provide the ionizing source for these nebulae, except in two instances, for which an early O star and a massive X-ray binary appear to provide the hard ionization, the former being especially puzzling. At present, the source of nebular He II 4686 is unexplained in Tol 89-B, whilst weak-lined WN or WC stars could provide the necessary hard ionizing photons in Tol 89-A.

We now consider the origin of the broad velocity components seen in knots A and B. They occur at the same velocity which suggests that they have a common origin, although the knot B component is narrower compared to that of knot A (70 vs. 110 km s^{-1}). In addition, the broad and narrow components appear to have a similar electron densities. This suggests that the gas responsible for the broad component can only be differentiated from the narrow H II region component by its width and that the two distinct components probably coexist within the GHR. Finally, we find that the maximum velocity of the gas, as measured by the FWZI, is 450–600 km s^{-1}.

Underlying broad components to nebular emission lines have been reported in a number of studies of GHRs, and WR and starburst galaxies (see Mendez & Esteban 1997; Homeier & Gallagher 1999, for a review). The properties of these components resemble those we have found in Tol 89; they have similar ionization conditions to the narrow components, and are spatially extended over the star-forming knots (Mendez & Esteban 1997). The origin of the broad component is not well understood; Homeier & Gallagher consider three possible explanations: (1) it is due to integrating over many ionized structures at different velocities; (2) it originates from hot, turbulent gas within superbubbles created by the winds from clusters; or (3) it is associated

with some type of break-out phenomenon such as a galactic wind. The third option is unlikely because the broad component is not velocity-shifted with respect to the narrow H II region component. The similar densities and ionization states of the broad and narrow components argues against the second option. We are then left with the first option that the broad component is the result of integrating over shell structures and filaments at different velocities. Studies of the well-resolved GHRs 30 Dor (Chu & Kennicutt 1994) and NGC 604 (Yang et al. 1996) show that their integrated profiles have low intensity broad wings due to fast expanding shells. We therefore favour this explanation because of the similar densities and ionization states of the broad and narrow components.

The narrower width of the broad component in knot B compared to knot A may be explained by the younger age of knot B (< 3 Myr compared to 4.5 Myr). The cluster winds in knot A will be more advanced than those in knot B because of the onset of WR winds and supernovae. We would thus expect the cluster winds in knot A to have had a larger impact on the dynamics and structure of the surrounding H II region. This is in accord with the larger reddening we deduce for knot B, its morphology showing a higher gas concentration (Fig. 4), as well as the fact that we observe velocity splitting in the main nebular component for knot A but not for knot B.

7.3 The massive star content of Tol 89

7.3.1 Clusters A1 to A4

We first consider the difference in the massive star contents of clusters A1 and A2. While A2 shows a mixed population of WN and WC stars, A1 only contains WN stars, although both have similar ages of 4.5 and 5.0 Myr. A similar difference in the populations of the two subclusters in the bright super–star cluster SSC-A in the dwarf starburst galaxy NGC 1569 was discussed by Maoz, Ho & Sternberg (2001). Their STIS long slit optical spectroscopy revealed the presence of young WR features ($\leqslant 5$Myr) coexisting with an older *red supergiant* (RSG) population ($\geqslant 4$Myr). Maoz et al. suggest that there is a dichotomy in the population of the two subclusters NGC 1569–A1 and A2, despite their similar ages of 5 Myr, in which the WR feature originates solely from NGC 1569–A2. They conclude that NGC 1569–A1 and A2 must have either widely different IMFs or widely different abundances, or similar, anomalously high, abundances but slightly different ages. In fact,

recent estimates of the age of NGC 1569-A2 have been revised and it is now believed to be around 12 Myr old (Anders et al. 2004), thus explaining the difference in the stellar populations of NGC 1569–A1 and A2. Of course, individual clusters can host mixed (WR and RSG) populations if their ages are in the range 4–5Myr. Westerlund 1 in the Milky Way is an example of a massive cluster whose content has been spatially resolved into RSG, WN and WC populations by Clark et al. (2005).

For the case of the clusters A1 and A2 in Tol 89 we find the difference between A1 containing only WN stars, and A2 both WN and WC stars, can be partially explained in terms of age effects due to the rapid evolution of WR stars on time scales of typically a few 10^5 years (Maeder & Meynet 1994). Since the WC phase follows the WN stage for the most massive stars, one might suspect that the slightly younger cluster (A1) contains only WN stars, while the older cluster (A2) contains a mixed population of WN stars and WC stars. Unfortunately, one expects the most massive stars to advance to the WC stage within ∼3Myr, which is inconsistent with the age inferred from the – A1 dominated – Hβ equivalent width in knot A. Alternatively, the age would need to exceed 5Myr for lower initial mass stars to advance through to the WN phase, but fail to become WC stars prior to core-collapse, which is also somewhat in conflict with the observed Hβ equivalent width for knot A. Differences in WR populations could result from variations in IMF, with a deficit in very high mass stars for A1, although this scenario appears to be rather contrived, given the rapid variation in N(WC)/N(WN) with age for young starbursts Schaerer & Vacca (1998).

A similar situation would appear to arise for clusters A3 and A4 in the sense that from their derived ages (see Section 4.1.2) one would also expect WR stars to be present. While no obvious WR signatures are detected in cluster A3, clear He II 1640 emission is observed in A4 (see Fig. 5). Remarkably, in cluster A4 we have been able to detect just three mid WN stars despite the large distance of 14.7 Mpc to Tol 89. The detection of such a small number of WR stars is partly made possible due to the weak continuum flux of this cluster, whose UV output is entirely dominated by these three WN stars. In contrast to cluster A4, the observed low S/N and stronger continuum in A3 may be masking any WR stars present in this cluster, thus we can not exclude the presence of a small number WN stars. We derive a mass for A3 and A4 of ∼ 0.4–1.7×10^4 and ∼ 1–5×10^3 M$_\odot$ from UV Starburst99 modelling. According to Cerviño & Mas-Hesse (1994) and Cerviño et al. (2002), below ∼ 10^{4-5} M$_\odot$ the IMF is no longer well sampled, thus affecting the integrated properties of the cluster. In such cases stellar population synthesis models can no longer be correctly applied (see e.g. Jamet et al. 2004). It is possible that the massive stellar content anomalies of A3 and A4 are due to a stochastic sampling of the IMF as a result of the low cluster masses.

7.3.2   *Empirical constraints*

Using template spectra of LMC WN and WC type stars (Crowther & Hadfield 2006) we have been able to derive consistent early WN (≈ 95) and WC (≈ 35) star numbers from both optical and UV diagnostics. In the UV, we sum the contributions from clusters A1 and A2 in order to make

direct comparisons with the optical UVES spectra of knot A; we do not include the three WN5–6 stars derived for cluster A4 since these will not contribute significantly to the optical blue bump which we attribute entirely to WN2–4 stars. Based on nebular derived O star populations, we estimate N(WR)/N(O) ∼0.2 for knot A, somewhat larger than single star evolutionary models predict at LMC metallicity Schaerer & Vacca (1998).

The UV STIS data are also presented in Chandar et al. (2004) who derive a He II 1640 flux equivalent to ∼ 130 early-type WN stars (based on the CH06 LMC line luminosity for WN2–4 stars) from their extraction of Tol 89-1 (encompassing our A1 and A2). This compares well to the results of this work, although we note that the difference is most likely due to the choice of extinction law used by Chandar et al. As noted by Hadfield & Crowther (2006), the use of a standard starburst extinction law is ideally suited to spatially unresolved galaxies. For extragalactic stellar clusters such as Tol 89-A1(–A3) and NGC 3125-A1, an LMC or SMC extinction law is more appropriate. Hadfield & Crowther (2006) have shown that the WR content of NGC 3125-1 derived from He II 1640 by Chandar et al. is strongly overestimated due to their choice of extinction law.

The absolute WR content we derive from the optical is significantly lower than that estimated by Schaerer et al. by about a factor of 3; although the WC/WN ratios obtained are in good agreement (cf ∼ 0.5 and ∼ 0.6 respectively). This discrepancy is likely due to several factors, including different adopted internal extinctions, slit widths (cf 1″6 to our 1″4) and position angle (PA 39° and 90°). Note that Schaerer et al. adopt the global extinction value derived for Tol 89 by Terlevich et al. (1991) (0.12 mags), whilst we derive an extinction value of zero mags for Tol 89-A directly.

7.3.3   *Starburst99 model constraints*

In Section 6.2 we compared three SB99+UCL models to the observed WR profiles in knot A; *1)* Solar; *2)* LMC with $\dot{M} - Z$ for WR stars switched on; and *3)* LMC with $\dot{M} - Z$ for WR stars switched off. Fig. 15 shows that while we are able to obtain good fits to the yellow WR bump, the fit to the blue bump is rather unsatisfactory – particularly in the case of the LMC metallicity models. The best agreement is achieved for solar metallicity models, which we acknowledge to be unphysical in view of the low metallicity of Tol 89.

Using the LMC models, the predicted number of WR stars is in reasonable agreement with the empirical results, approximately a factor of ∼ 1–2 times smaller (cf ∼ 60–90 to 130), while the O-star numbers are also similar from the stellar continuum (∼ 660–910) and H II region (∼ 690) analyses respectively. The SB99+UCL spectral synthesis models predict N(WR)/N(O) ∼ 0.1 versus ∼ 0.2 from direct stellar (WR) and indirect nebular (O) results. Unfortunately, the major failure of the spectral synthesis approach relates to the distribution of WR stars, which is observed to be primarily WN stars in contrast to a predicted dominant WC population. As a consequence, the fit to the blue bump is poor since the WN population is greatly underestimated.

However, let us recall that non-rotating evolutionary models are at present used in Starburst99 synthesis models. Meynet & Maeder (2003, 2005) have shown that the inclusion of rotational mixing in their evolutionary models

increases the WR lifetimes – mainly as a result of the increased duration of the H-rich phase – and lowers the initial mass limit for the formation of WR stars. The combination of these two factors is to decrease the N(WC)/N(WN) ratio and increase the predicted N(WR)/N(O) ratio, bringing predictions closer to our empirical results for Tol 89-A. The potential use of synthetic WR line bumps in Starburst99 models as diagnostics of WR populations is at present severely hindered by the lack of rotational mixing in evolutionary models. Until then, one should treat detailed N(WR)/N(O) and WR subtype distributions predicted by such models with caution.

8   SUMMARY

We have presented new high spectral resolution VLT/UVES spectroscopy and archival HST/STIS imaging and spectroscopy of the giant H II region Tol 89 in NGC 5398.

From optical HST/STIS imaging we resolve the two brightest optical knots of star formation, Tol 89-A and B, into individual, young compact massive clusters A1–4 and B1 ($R_{eff} \leqslant 3$ pc, M $>\sim 10^{3-5}$ M$_\odot$). We derive ages for knots A and B of ~ 4.5 and < 3 Myr respectively. We determine a mass from Starburst99 modelling for the brightest cluster in A (A1) of ~ 1–2×10^5 M$_\odot$. A total mass of $\sim 6 \times 10^5$ M$_\odot$ is inferred for the ionizing sources at the heart of knot B. A further two young compact massive clusters ($R_{eff} < 2$ pc; C1 and C2) are identified in the STIS UV image which may also fall into the SSC (mass) category. In total, we identify at least seven young massive compact clusters in the Tol 89 star-forming complex. We find that the GHR properties of Tol 89 are similar to the three GHRs in M101 and 30 Dor. Tol 89, however, contains six clusters of SSC proportions whereas the other four comparison GHRs do not. Tol 89 is therefore exceptional in terms of its cluster content and its isolated location in the late-type galaxy NGC 5398.

In agreement with the results of Schaerer et al. 1999, we show that the WR emission is localised to the region with maximum stellar continuum, knot A; while STIS UV spectroscopy reveals that the WR stars are confined to clusters A1, A2 and A4, with early WC stars located only in A2. We have modelled the observed WR line profiles using the empirical template spectra of LMC WN and WC stars presented in Crowther & Hadfield (2006), revealing ~ 95 early WN stars and ~ 35 WC stars in Tol 89-A. WR populations inferred from our empirical technique are consistent between optical and UV diagnostics, and so are well constrained. For clusters A1, A2 and A4, we obtain N(WC)/N(WN) ~ 0, ~ 3 and ~ 0, respectively. It is feasible that the slight difference in ages of clusters A1 and A2 (cf ~ 4.5 and ~ 5 Myr respectively) is responsible for this difference in their massive star population, although differences in IMF cannot be excluded. In cluster A4 we have been able to detect three mid WN stars despite the large distance to Tol 89, which is testament to the dominance of WR stars at UV wavelengths. The detection of so few WN stars may be the result of stochastic sampling of the IMF. From nebular Hβ emission, we obtain N(O)~ 690 and 2800 for knots A and B, from which we infer N(WR)/N(O)~ 0.2 for the former region. For knot B, N(O) is a factor of two smaller than recent radio observations by Johnson et al. (2003).

We have constructed complementary Starburst99 (Leitherer et al. 1999) models in which optical spectral synthesis of WR stars has been implemented using the UCL WR star grids of Smith et al. (2002). O star populations from optical continuum flux distributions are in good agreement with nebular results, although the SB99 + UCL models fail to reproduce the observed strength of the blue WR bump, because too few WN stars are predicted in the evolutionary models. The inclusion of evolutionary tracks with rotational mixing (Meynet & Maeder 2003, 2005) should help to resolve this issue by increasing the lifetime of WNs during the H-rich phase. Nevertheless, the total WR populations obtained in this way agree with the empirical results to within a factor of 2–3.

From an analysis of the optical nebular emission lines, we confirm previous determinations that Tol 89 has an LMC-type metallicity. Nebular He II 4686 is observed in Tol 89–B and perhaps Tol 89–A from UVES and STIS spectroscopy. The latter is expected for early-type WR populations at low metallicity, whilst He II 4686 emission from starburst regions prior to the WR stage is not predicted, unless this is formed within a shocked region surrounding young O star populations, as may be the case for N44C in the LMC. We detect symmetrical broad components in the strongest nebular lines with velocities up to 450–600 km s^{-1}. We find that this high velocity gas has similar properties to the H II gas as revealed by the narrow components, and suggest that it is the result of integrating over shell structures and filaments at different velocities within the GHR.

REFERENCES

Anders P., de Grijs R., Fritze-v. Alvensleben U., Bissantz N., 2004, MNRAS, 347, 17
Ashman K. M., Zepf S. E., 1992, ApJ, 384, 50
Bastian N., Gieles M., Efremov Y. N., Lamers H. J. G. L. M., 2005, A&A, 443, 79

Bastian N., Saglia R. P., Goudfrooij P., Kissler-Patig M., Maraston C., Schweizer F., Zoccali M., 2006, A&A, 448, 881

Calzetti D., Armus L., Bohlin R. C., Kinney A. L., Koornneef J., Storchi-Bergmann T., 2000, ApJ, 533, 682

Cerviño M., Mas-Hesse J. M., 1994, A&A, 284, 749

Cerviño M., Valls-Gabaud D., Luridiana V., Mas-Hesse J. M., 2002, A&A, 381, 51

Chandar R., Leitherer C., Tremonti C. A., 2004, ApJ, 604, 153

Chen C.-H. R., Chu Y., Johnson K. E., 2005, ApJ, 619, 779

Chu Y.-H., Kennicutt R. C., 1994, ApJ, 425, 720

Clark J. S., Negueruela I., Crowther P. A., Goodwin S. P., 2005, A&A, 434, 949

Crowther P. A., de Marco O., Barlow M. J., 1998, MNRAS, 296, 367

Crowther P. A., Dessart L., 1998, MNRAS, 296, 622

Crowther P. A., Hadfield L. J., 2006, A&A

Crowther P. A., Hillier D. J., Evans C. J., Fullerton A. W., De Marco O., Willis A. J., 2002, ApJ, 579, 774

Crowther P. A., Smith L. J., 1996, A&A, 305, 541

de Mello D. F., Leitherer C., Heckman T. M., 2000, ApJ, 530, 251

D'Odorico S., Cristiani S., Dekker H., Hill V., Kaufer A., Kim T., Primas F., 2000, in Proc. SPIE Vol. 4005, p. 121-130, Discoveries and Research Prospects from 8- to 10-Meter-Class Telescopes, Jacqueline Bergeron; Ed. Performance of UVES, the echelle spectrograph for the ESO VLT and highlights of the first observations of stars and quasars. pp 121–130

Durret F., Bergeron J., Boksenberg A., 1985, A&A, 143, 347

Elmegreen B. G., Efremov Y. N., 1997, ApJ, 480, 235

Garnett D. R., Kennicutt R. C., Chu Y.-H., Skillman E. D., 1991, PASP, 103, 850

Girardi L., Bressan A., Bertelli G., Chiosi C., 2000, A&A, 141, 371

Guseva N. G., Izotov Y. I., Thuan T. X., 2000, ApJ, 531, 776

Hadfield L. J., Crowther P. A., 2006, MNRAS

Heap S. R., Lanz T., Hubeny I., 2006, ApJ, 638, 409

Hillier D. J., Miller D. L., 1998, ApJ, 496, 407

Holtzman J. A., Faber S. M., Shaya E. J., Lauer T. R., Groth J., Hunter D. A., Baum W. A., Ewald S. P., Hester J. J., Light R. M., Lynds C. R., O'Neil E. J., Westphal J. A., 1992, AJ, 103, 691

Homeier N. L., Gallagher J. S., 1999, ApJ, 522, 199

Howarth I. D., 1983, MNRAS, 203, 301

Hunter D. A., Baum W. A., O'Neil E. J., Lynds R., 1996, ApJ, 456, 174

Hunter D. A., Shaya E. J., Holtzman J. A., Light R. M., O'Neil E. J., Lynds R., 1995, ApJ, 448, 179

Izotov Y. I., Thuan T. X., Lipovetsky V. A., 1994, ApJ, 435, 647

Jamet L., Pérez E., Cerviño M., Stasińska G., González Delgado R. M., Vílchez J. M., 2004, A&A, 426, 399

Johnson K. E., Indebetouw R., Pisano D. J., 2003, AJ, 126, 101

Kennicutt R. C., 1984, ApJ, 287, 116

Kennicutt R. C., 1998, Ann. Rev. Astr. Astrophys., 36, 189

Kennicutt R. C., et al. 2003, PASP, 115, 928

Kennicutt R. C., Lee J. C., Funes J. G., Sakai S., Akiyama

S., 2005, in de Grijs R., González Delgado R. M., eds, ASSL Vol. 329: Starbursts: From 30 Doradus to Lyman Break Galaxies Demographics and Host Galaxies of Starbursts. pp 187–+

King I., 1962, AJ, 67, 471

Kroupa P., 2001, MNRAS, 322, 231

Larsen S. S., 1999, A&AS, 139, 393

Larsen S. S., 2004, A&A, 416, 537

Larsen S. S., Richtler T., 1999, A&A, 345, 59

Larsen S. S., Richtler T., 2000, A&A, 354, 836

Leitherer C., Leão J. R. S., Heckman T. M., Lennon D. J., Pettini M., Robert C., 2001, ApJ, 550, 724

Leitherer C., Schaerer D., Goldader J. D., Delgado R. M. G., Robert C., Kune D. F., de Mello D. F., Devost D., Heckman T. M., 1999, ApJSS, 123, 3

Liu X.-W., Storey P. J., Barlow M. J., Danziger I. J., Cohen M., Bryce M., 2000, MNRAS, 312, 585

Maeder A., Meynet G., 1994, A&A, 287, 803

Maoz D., Ho L. C., Sternberg A., 2001, ApJL, 554, L139

Maraston C., Bastian N., Saglia R. P., Kissler-Patig M., Schweizer F., Goudfrooij P., 2004, A&A, 416, 467

Martins F., Schaerer D., Hillier D. J., 2005, A&A, 436, 1049

Martins L. P., Delgado R. M. G., Leitherer C., Cerviño M., Hauschildt P., 2005, MNRAS, 358, 49

Massey P., Puls J., Pauldrach A. W. A., Bresolin F., Kudritzki R. P., Simon T., 2005, ApJ, 627, 477

Melnick J., Tenorio-Tagle G., Terlevich R., 1999, MNRAS, 302, 677

Mendez D. I., Esteban C., 1997, ApJ, 488, 652

Meynet G., Maeder A., 2003, A&A, 404, 975

Meynet G., Maeder A., 2005, A&A, 429, 581

Meynet G., Maeder A., Schaller G., Schaerer D., Charbonnel C., 1994, A&AS, 103, 97

Peimbert A., 2003, ApJ, 584, 735

Pellerin A., 2006, AJ, 131, 849

Robert C., Leitherer C., Heckman T. M., 1993, ApJ, 418, 749

Rubin R. H., 1986, ApJ, 309, 334

Russell S. C., Dopita M. A., 1990, ApJSS, 74, 93

Schaerer D., Contini T., Kunth D., 1999, A&A, 341, 399

Schaerer D., Contini T., Pindao M., 1999, A&AS, 136, 35

Schaerer D., Vacca W. D., 1998, ApJ, 497, 618

Schlegel D. J., Finkbeiner D. P., Davis M., 1998, ApJ, 500, 525

Schmutz W., Leitherer C., Gruenwald R., 1992, PASP, 104, 1164

Schweizer F., Seitzer P., 1998, AJ, 116, 2206

Seaton M. J., 1979, MNRAS, 187, 73P

Shields G. A., 1990, Ann. Rev. Astr. Astrophys., 28, 525

Smith L. J., Norris R. P. F., Crowther P. A., 2002, MNRAS, 337, 1309

Smith M. G., Aguirre C., Zemelman M., 1976, ApJSS, 32, 217

Terlevich R., Melnick J., Masegosa J., Moles M., Copetti M. V. F., 1991, A&AS, 91, 285

Vacca W. D., 1994, ApJ, 421, 140

van Dokkum P. G., 2001, PASP, 113, 1420

Vázquez G. A., Leitherer C., 2005, ApJ, 621, 695

Whitmore B. C., 2003, in A Decade of Hubble Space Telescope Science The formation of star clusters. pp 153–178

Whitmore B. C., Miller B. W., Schweizer F., Fall S. M., 1997, AJ, 114, 1797

Yang H., Chu Y.-H., Skillman E. D., Terlevich R., 1996,
   AJ, 112, 146

This paper has been typeset from a TeX/ LaTeX file prepared
by the author.